Pacific Northwest
NATIONAL LABORATORY

PNNL-36939

Self-Aware Local Autonomous and Semi-Cooperative Control for Cross-Layered Resilience (SLAC3R)

Technical Report

November 14, 2024

Sai Pushpak Nandanoori
Sandip Roy
Jean-Baptiste Bouvier
Soumya Kundu
Ankit Singhal
Alok Kumar Bharati
Subhrajit Sinha
Wenceslao Shaw Cortez
Veronica Adetola

U.S. DEPARTMENT OF ENERGY

Prepared for the U.S. Department of Energy
Under contract DE-AC05-76RL01830

DISCLAIMER

PACIFIC NORTHWEST NATIONAL LABORATORY
operated by
BATTELLE
for the
UNITED STATES DEPARTMENT OF ENERGY
under Contract DE-AC05-76RL01830

Printed in the United States of America

Available to DOE and DOE contractors from
the Office of Scientific and Technical Information,
P.O. Box 62, Oak Ridge, TN 37831-0062
www.osti.gov
ph: (865) 576-8401
fox: (865) 576-5728
email: reports@osti.gov

Available to the public from the National Technical Information Service
5301 Shawnee Rd., Alexandria, VA 22312
ph: (800) 553-NTIS (6847)
or (703) 605-6000
email: info@ntis.gov
Online ordering: http://www.ntis.gov

PNNL-36939

Self-Aware Local Autonomous and Semi-Cooperative Control for Cross-Layered Resilience (SLAC3R)

Technical Report

November 14, 2024

Sai Pushpak Nandanoori
Sandip Roy
Jean-Baptiste Bouvier
Soumya Kundu
Ankit Singhal
Alok Kumar Bharati
Subhrajit Sinha
Wenceslao Shaw Cortez
Veronica Adetola

Prepared for
the U.S. Department of Energy
Under Contract DE-AC05-76RL01830

Pacific Northwest National Laboratory
Richland, Washington 99352

Acronyms and Abbreviations

SLAC3R	Self-Aware Local Autonomous and Semi-Cooperative Control for Cross-Layered Resilience
PNNL	Pacific Northwest National Laboratory

Acknowledgments

This work was carried out (contract DE-AC05-76RL01830) under the support from the U.S. Department of Energy Office of Electricity as part of the PNNL-LDRD RD2C Initiative.

Contents

Figures

Tables

1.0 Proactive Autonomy

The massive failure of the Texas electrical grid in February 2021 [3] gave global coverage to the issue of power network resilience. During these extreme events, time and resources are of essence for the grid operator to assess the situation and take appropriate actions to maintain the operating state of the power network. Hence, to an extent it is imperative on the grid operator to be prepared for extreme events. Microgrids, both grid-connected and stand-alone, have shown promise to enhance resilience and reliability by paving a way of coordinating multiple distributed energy resources (DERs) as a locally operated single controllable entity [4, 5]. However, ensuring operational stability, safety, and reliability of any power network involves a complex multi-timescales problem, spanning sub-seconds to minutes and hours. Traditional power system control operations were largely structured around a temporal decoupling which allows slower-timescale operations (e.g., optimal dispatch) need not directly take into account faster-timescale constraints, and *vice versa*. However, with the emergence of inverter-based DERs and the associated changes in power systems dynamics (e.g., reducing inertia), the timescales separation is expected to continue to shrink [6]. The droop-controlled inverter based microgrids have a lower inertia than conventional generators, which allows large variations of the voltage and frequency of each inverters [5, 7]. The fluctuations happen during the transient evolution occurring as a result of a fault or due to the transitions between the power set-points, and can lead to violation of safety constraints [8]. It is imperative to develop a mechanism to inform slower-timescale operations (e.g., optimal dispatch of power set-points) of the constraints arising from faster-timescale (transient) dynamics.

Many recent efforts have addressed this need via, for example, stability and security-constrained optimization [5, 7, 9], identification of local and distributed parametric stability conditions [8, 10, 11], etc. The distributed identification of stability conditions are particularly interesting since these fit well into a multi-ownership models of microgrid resources, and facilitate hierarchical and plug-and-play operations [12]. However, most of the related literature, as above, only focus on the stability which concerns with the convergence of power system trajectories (close) to its normal operating point after a disturbance. The concept of safety, on the other hand, relates to avoiding critical operational limits (e.g., on voltages and frequencies), even under large disturbances. Safety is closely tied to resilience, since often in cyber-physical adversarial scenarios, an immediate priority is to contain the system trajectories within some acceptable set, rather than ensuring return to normality.

Safety-constrained control techniques are gaining recent attention in the power systems community [13–16]. Model-predictive control [17] remains one of the most commonly used methods for enforcing dynamic constraints over some prediction horizon. However, it suffers from certain limitations in the context of power system dynamics, related to, for example, nonlinearity and associated complexity of the dynamics, information disparity due to communication overheads and/or privacy concerns, and computational burden, especially for longer prediction horizon [15]. To circumvent these issues, distributed safety verification and control methods based on robust forward set-invariance principles have been proposed in [13–16]. However, these prior works rely on the existence or the construction of parametric Lyapunov functions and/or barrier functions, thereby often incurring prohibitive computational costs and resulting in conservative safety certificates. The work in [13], for example, proposes a sum-of-squares (SOS) programming based computation algorithm for distributed safety certificates as a super-level set of barrier functions. However, such computational methods result in conservative estimates of the safety-guaranteed set (e.g., Fig. 1 in [13]), and typically do not scale well.

In this work, we consider a hierarchical and modular microgrid control architecture, [12, 16, 18], which allows system-level dispatch of power set-points to inverter-based resources, accommodating only limited data exchange between the (neighboring) inverter modules. Our objective is

to design bounds on dispatched control set-points at the inverter buses, that guarantee, in a distributed sense, the safe excursions of local voltage and frequency within the specified limits while tolerating uncertainty in the neighboring buses. Specifically, the work presented in this report relies on the *Nagumo's theorem* [19,20] to build an efficient method for distributed and robust safety verification, without requiring existence or construction of barrier functions. Thus, the proposed approach requires less computation, and relaxes the conservativeness of the barrier-certified safe sets by directly accommodating the original safety specifications. The explicit reference governor [21] relies on the same concept but we focus on establishing safe bounds on control inputs, instead of deriving a specific control law, which is the role of the grid coordinator [16].

The main contributions of this article are threefold. Firstly, we determine the maximal interval (bounds) of the dispatched control set-points guaranteeing the safety of droop-controlled inverters. Secondly, we establish the monotonic relationship between this interval of safety admissible control set-points and the droop coefficients. Finally, we calculate efficiently the maximal droop coefficient for which these safety admissible controls exist. As such, this report provides novel design guidelines for the droop control parameters, extending the literature on stability-informed droop settings, e.g., [8, 10, 11], and the references therein. We use SOS programming to solve the safety verification problems, and illustrate the algorithm via numerical simulations.

1.1 Preliminaries

1.1.1 Invariant Sets

Consider a nonlinear dynamical system of the form

$$\dot{x}(t) = f\big(x(t)\big), \qquad x \in \mathbb{R}^n, \tag{1}$$

with f a Lipschitz continuous function. The objective of our work is to identify safe sets that the state x cannot leave. Such sets are called *invariant* (or *positively invariant*); we define them as in [20].

Definition 1 *A set S is* invariant *by the dynamics* (1) *if $x(0) \in S$ yields $x(t) \in S$ for all $t \geq 0$.*

To characterize invariant sets we will be using a theorem first established by Nagumo [19] and then independently rediscovered by Brezis [22]. We state here a more modern formulation of this result from [20].

Theorem 1 (Nagumo 1942) *A closed set S is invariant by the dynamics* (1) *if and only if for all $x \in S$, $f(x) \in \mathcal{C}(x)$, with $\mathcal{C}(x)$ the Bouligand tangent cone to S at x.*

A full definition of the Bouligand tangent cone is given in [20], but we will be studying sets S where the Bouligand tangent cone is $\mathbb{R}^+$ or $\mathbb{R}^-$. The geometrical interpretation of Nagumo's theorem is that f pointing inside S on its boundary prevents trajectories from leaving S.

1.1.2 Network Safety

In a network, the dynamics of node i can be modeled by

$$\dot{x}_i(t) = f_i\big(x_i(t), u_i(t), w_i(t)\big),\ x_i \in \mathbb{R}^n,\ u_i \in U,\ w_i \in W, \tag{2}$$

with u_i a control input, w_i an external input, and U and W their respective admissible sets. For such a system we need to adapt our definition of invariant sets following [20].

Definition 2 *A set S is* robust control invariant *by the dynamics* (2) *if there exists a feedback control law $u_i(t)$ such that for all $x_i(0) \in S$ and all time-varying $w_i \in W$, $x_i(t) \in S$ for all $t \geq 0$.*

We then want to determine the set of control inputs u ensuring the robust control invariance of a given safe set S despite the fluctuations in the neighboring inverter states. In particular, specific to the example of inverter-based microgrids, i.e., when the safe sets are expressed as box constraints on the states (as in (6)), we define the following:

Definition 3 *A 1-dimensional set $S = [\underline{s}, \overline{s}]$ is* upper invariant *(resp.* lower invariant*) for a set of controls U by the dynamics* (2) *if for all time-varying $w \in W$, $u \in U$ and all $x(0) \in S$, then $x(t) \leq \overline{s}$ (resp. $x(t) \geq \underline{s}$) for $t \geq 0$.*

If S is upper invariant (resp. lower invariant), then the state cannot escape by crossing the upper bound (resp. lower bound) of S. Notice that if there are controls making S both upper and lower invariant, then S is a robust control invariant set. We denote such controls as *safety admissible*.

Definition 4 *A set of controls U is* safety admissible *for the set S if for all controls $u \in U$, the set S is robust control invariant.*

As we will detail later, if the dynamics (2) and the safe set S are polynomial, e.g.,

$$S = \left\{x \in \mathbb{R}^n : p_j(x) \ \geq \ 0, j \ \in \ \{1, \ldots, m\}\right\}$$

with p_j polynomials, then the invariance condition of Nagumo's theorem can be stated as a polynomial inequality, enabling its fast computation.

1.2 Problem Description

A microgrid power network is operated by a microgrid coordinator that determines power setpoints for each node of the grid [16, 18]. The transition in between these setpoints, corresponding to a transient regime, might lead the frequency or voltage of some inverters to violate safety constraints. We are thus interested in ensuring the transient safety of microgrid networks, so that they are reliable when operated. Consider the case of droop-controlled inverters [8]:

$$\dot{\theta}_i = \omega_i, \tag{3a}$$

$$\tau_i \dot{\omega}_i = -\omega_i + \lambda_i^p \left(P_i^{set} - P_i\right), \tag{3b}$$

$$\tau_i \dot{v}_i = v_i^0 - v_i + \lambda_i^q \left(Q_i^{set} - Q_i\right), \tag{3c}$$

where θ_i, ω_i and v_i are, respectively, the phase angle, frequency and voltage magnitude of node i. The droop-coefficients $\lambda_i^p > 0$ and $\lambda_i^q > 0$ are associated with the active power vs. frequency and the reactive power vs. voltage droop curves, respectively. The time-constant of the low-pass filter used for the active and reactive power measurements is τ_i. The nominal voltage magnitude is v_i^0. The active power and reactive power set-points are P_i^{set} and Q_i^{set}, respectively. Finally, the active and reactive power injected into the network are P_i and Q_i, respectively following the nonlinear coupling equations

$$P_i = v_i \sum_{k \in \mathcal{N}_i} v_k (G_{i,k} \cos \theta_{k,i} - B_{i,k} \sin \theta_{k,i}), \tag{4a}$$

$$Q_i = -v_i \sum_{k \in \mathcal{N}_i} v_k (G_{i,k} \sin \theta_{k,i} + B_{i,k} \cos \theta_{k,i}), \tag{4b}$$

where $\theta_{k,i} = \theta_k - \theta_i$, and $\mathcal{N}_i$ is the set of neighbor nodes with the convention that $i \in \mathcal{N}_i$. The transfer conductance and susceptance of the line connecting nodes i and k are denoted by $G_{i,k}$ and $B_{i,k}$, respectively.

We use the formulation of [13] to model the capability of the inverters to change their control set-points of the active and reactive power output in order to adjust to different operating conditions. More specifically, we write

$$P_i^{set} = P_i^0 + u_i^p, \quad \text{and} \quad Q_i^{set} = Q_i^0 + u_i^q, \tag{5}$$

where P_i^0 and Q_i^0 are the set-points for the nominal operating conditions; and u_i^p and u_i^q are control inputs. We are thus interested in maintaining at all times both voltage and frequency within some pre-specified safety limits. By a usual abuse of notation, instead of considering the actual voltage, we consider its difference from the nominal voltage $v_i^0 = 1$ p.u.. Following [13,23,24], we consider the voltage and frequency safe sets to be

$$S_v = [\underline{v}, \overline{v}] = [-0.4, 0.2]\,\text{p.u.}\,, \tag{6a}$$
$$S_\omega = [\underline{\omega}, \overline{\omega}] = [-3, 3]\,\text{Hz}\,. \tag{6b}$$

For the inverters (3), the perturbation w_i from Definition 2 are the neighbor voltage magnitudes (v_k) and phase angle differences ($\theta_{k,i}$) that determine the power transfers, P_i and Q_i. For the purpose of this report, we assume that the phase angle differences between (any) two neighbor buses are bounded as follows:

$$\theta_{i,k} \in S_\theta = [-\pi/6, \pi/6] \quad \forall k \in \mathcal{N}_i\,. \tag{7}$$

Note that such range of phase angle differences are typical of distribution feeders, and especially microgrids, that are often characterized by relatively short lines connecting two buses [25]. Furthermore, note that only the difference of phase angles θ_i and θ_k as opposed to their individual values, determine the power-flow connecting the nodes i and k. Thus, for simplicity to notations and without any loss of generality, we set $\theta_i \equiv 0$ as the *reference angle*, and use $\theta_{k,i} \equiv \theta_k$ throughout this text. Then, we want to determine controls $u_i = (u_i^p, u_i^q)$ that maintain $v_i \in S_v$ and $\omega_i \in S_\omega$, whatever the values of $\theta_k \in S_\theta$ and $v_k \in S_v$ for the neighbors $k \in \mathcal{N}_i$.

Problem 1 *(Safety-Admissible Control) What values of control set-points u_i ensure that S_v and S_ω are robust control invariant by the dynamics* (3)*?*

Moreover, note that the impact of neighbor (and network) disturbances on the inverter dynamics (3) are enhanced by larger droop values, a fact which suggests the existence and size of the *safety-admissible* controls depend on the chosen droop coefficients. This motivates the following question:

Problem 2 *(Maximal Droop) What values of droop coefficients $(\lambda_i^p, \lambda_i^q)$ ensure the existence of a non-empty safety-admissible set of controls, guaranteeing robust control invariance of S_v and S_ω as per dynamics* (3)*?*

1.3 Theoretical Construction

In this section we establish the theory concerning robust control invariant sets for droop-controlled inverters. Since $\lambda_i^p > 0$ and $\lambda_i^q > 0$ in the inverter dynamics (3), we can define a *minimal lower*

control $\underline{u}$ and a *maximal upper control* $\overline{u}$ such that

$$\underline{u} = \inf\left\{u_{low} \in \mathbb{R} : S \text{ is lower invariant for all } u \geq u_{low}\right\},$$
$$\overline{u} = \sup\left\{u_{up} \in \mathbb{R} : S \text{ is upper invariant for all } u \leq u_{up}\right\}.$$

If $\underline{u} \leq \overline{u}$, then the maximal interval of safety admissible controls is $[\underline{u}, \overline{u}]$. To illustrate these definitions and our objective let us study a simplified version of (3).

1.3.1 Simple Example

Consider the frequency dynamics equation (3b) when the inverter has a single neighbor. To simplify take $\tau = 1$s, $\lambda^p = 1$rad/s/p.u., $\theta_2 = 0$rad, $P^0 = 0$p.u., $G = -2$p.u.$^{-1}$ and a safe set $S = [-1, 1]$Hz. Then, $\dot{\omega} = -\omega + 2\omega\omega_2 + u$.

To make S upper invariant, according to Nagumo's theorem we need $\dot{\omega} \leq 0$ when $\omega = 1$. Thus, we want $2\omega_2 - 1 + u \leq 0$, so $u \leq 1 - 2\omega_2$. We are looking for robust controls u working for all possible $\omega_2 \in S$. Then, the maximal upper control is $\overline{u} = -1$, because for $\omega_2 = 1$, we need $u \leq -1$.

Similarly, to make S lower invariant, we need $\dot{\omega} \geq 0$ when $\omega = -1$. Then, we want $-2\omega_2 + 1 + u \geq 0$, i.e., $u \geq -1 + 2\omega_2$. Thus, the minimal lower control is $\underline{u} = 1$.

In this setting, $\overline{u} < \underline{u}$, there are no safety admissible controls making S robust control invariant. A reason for this failure is that λ^p is too large, making ω unstable. Indeed, for small values of λ^p, (3b) can be approximated by $\tau_i\dot{\omega}_i = -\omega_i$ which is stable. We will elaborate further on this issue in the following subsections.

1.3.2 Minimal controls for upper and lower invariance

Let us determine the minimal lower control for S_ω. By definition, $\underline{u_i^p} = \inf\limits_{\theta_k, v_k} \{u_i^p : \dot{\omega}_i \geq 0,\ \omega_i = \underline{\omega}\}$. With (3b), $\underline{u_i^p} = \inf\left\{u_i^p : u_i^p \geq \frac{1}{\lambda_i^p}\underline{\omega} + P_i - P_i^0,\ \forall\theta_k, v_k\right\}$. Then, the minimal u_i^p that is larger than all $\left[\frac{1}{\lambda_i^p}\underline{\omega} + P_i - P_i^0\right](\theta_k, v_k)$ is in fact the maximum of this term over all θ_k and v_k, because P_i is continuous in θ_k, v_k according to (4a) and, S_θ and S_v are compact. Thus,

$$\begin{aligned} \underline{u_i^p} = &\max_{\theta_k, v_k} \frac{1}{\lambda_i^p}\underline{\omega} + P_i - P_i^0, \\ &\text{subject to} \quad \theta_k \in S_\theta,\ v_k \in S_v,\ k \in \mathcal{N}_i, \end{aligned} \tag{8}$$

Then, $\dot{\omega}_i \geq 0$ when $\omega_i = \underline{\omega}$ and $u_i^p \geq \underline{u_i^p}$ for all $\theta \in S_\theta$ and $v \in S_v$, which guarantees lower invariance according to Nagumo's theorem. Similarly, the maximal upper control is defined as

$$\begin{aligned} \overline{u_i^p} = &\min_{\theta_k, v_k} \frac{1}{\lambda_i^p}\overline{\omega} + P_i - P_i^0, \\ &\text{subject to} \quad \theta_k \in S_\theta,\ v_k \in S_v,\ k \in \mathcal{N}_i, \end{aligned} \tag{9}$$

and makes $\dot{\omega}_i \leq 0$ when $\omega_i = \overline{\omega}$ and $u_i^p \leq \overline{u_i^p}$ for all $\theta \in S_\theta$ and $v \in S_v$. The minimal lower control $\underline{u_i^q}$ and maximal upper control $\overline{u_i^q}$ for the voltage equation are defined similarly.

A great way to solve the optimization problems (8) and (9) is to use a sum-of-squares (SOS) optimization. A multivariate polynomial $p(x)$, $x \in \mathbb{R}^n$, is an SOS if there exist polynomial functions $h_i(x)$, $i = 1, \ldots, s$ such that $p(x) = \sum_{i=1}^s h_i^2(x)$. However, the power-flow equations (4) are not polynomials. Following [13] we choose a third order Taylor expansion of the dynamics (4) to make (3) polynomial. Then, (8) and (9) can be solved with any SOS tool.

1.3.3 Maximal droop for robust control invariance

The stability of the voltage and frequency rely on small droop coefficients λ. As in Section 1.3.1, when λ increases in (3), the perturbations P and Q increase, and we thus have the intuition that the set of safety admissible controls should shrink. We can actually prove a stronger result by using the fact that the optimizations in (8) and (9) only affect P_i.

Proposition 1 *The bounds of the interval of safety admissible controls $[\underline{u}, \overline{u}]$ for S_v and S_ω are inversely proportional to the droop coefficient λ.*

Proof. We first introduce the maximum and minimum of the active and reactive powers (4) at the lower and upper bounds of S_ω and S_v. More specifically

$$\begin{aligned}
P_i^{max} &= \max\left\{P_i : \omega_i = \underline{\omega},\ (\theta_k, v_k) \in S_\theta \times S_v,\ k \in \mathcal{N}_i\right\},\\
P_i^{min} &= \min\left\{P_i : \omega_i = \overline{\omega},\ (\theta_k, v_k) \in S_\theta \times S_v,\ k \in \mathcal{N}_i\right\},\\
Q_i^{max} &= \max\left\{Q_i : v_i = \underline{v},\ (\theta_k, v_k) \in S_\theta \times S_v,\ k \in \mathcal{N}_i\right\},\\
Q_i^{min} &= \min\left\{Q_i : v_i = \overline{v},\ (\theta_k, v_k) \in S_\theta \times S_v,\ k \in \mathcal{N}_i\right\}.
\end{aligned}$$

Then, (8) and (9) simplify to

$$\underline{u_i^p}(\lambda_i^p) = \frac{1}{\lambda_i^p}\underline{\omega} + P_i^{max} - P_i^0,\ \ \overline{u_i^p}(\lambda_i^p) = \frac{1}{\lambda_i^p}\overline{\omega} + P_i^{min} - P_i^0. \tag{10}$$

A similar result holds for the voltage. ■

Building on this result, we can then establish a sufficient condition for the existence of safety admissible controls.

Proposition 2 *If the safe set contains 0 in its interior, then safety admissible controls exist for some droop coefficients.*

Proof. Note that ω_i does not intervene in P_i (4a), so the constraints for P_i^{min} and P_i^{max} are the same, which leads to $P_i^{min} < P_i^{max}$. Then, based on (10), the condition $\underline{\omega} < 0 < \overline{\omega}$ is necessary and sufficient to make $\underline{u_i^p}(\lambda_i^p) < \overline{u_i^p}(\lambda_i^p)$ for λ_i^p small enough.

On the other hand, since v_i intervenes in Q_i (4b), we cannot order Q_i^{min} and Q_i^{max} without computing them. Thus the condition $\underline{v} < 0 < \overline{v}$ is sufficient but maybe not necessary to make $\underline{u_i^q}(\lambda_i^q) < \overline{u_i^q}(\lambda_i^q)$ for some λ_i^q. ■

Then, the safe sets of (6) guarantee that safety admissible controls exist for some small enough droop coefficients. We now want to find the maximal droop coefficient λ^* for which safety admissible controls exist, i.e.,

$$\lambda^* = \max\left\{\lambda \geq 0 : \underline{u}(\lambda) \leq \overline{u}(\lambda)\right\}. \tag{11}$$

Remark 1 *Note that the problem of identifying the maximal droop for stability analysis is relatively well studied in the literature (see, for instance, [8, 10, 11]). However, as a novel contribution of this report, we propose a method to identify maximal droop values for safety verification.*

According to Proposition 1 and 2, if 0 is in the interior of S and $\lambda \leq \lambda^*$, then the interval $[\underline{u}(\lambda), \overline{u}(\lambda)]$ is not empty, is proportional with $1/\lambda$ and makes S robust control invariant,.

Proposition 3 *The maximal droop coefficient λ^* is*

$$\lambda_i^{p*} = \frac{\overline{\omega} - \underline{\omega}}{P_i^{max} - P_i^{min}} \quad \textit{and} \quad \lambda_i^{q*} = \frac{\overline{v} - \underline{v}}{Q_i^{max} - Q_i^{min}}. \tag{12}$$

Proof. Since $\underline{u_i^p}$ and $\overline{u_i^p}$ are continuous in λ_i^p according to (10), definition (11) leads to $\underline{u_i^p}(\lambda_i^{p*}) = \overline{u_i^p}(\lambda_i^{p*})$. Using (10) we easily obtain the announced expression for λ_i^{p*}. The calculation of λ_i^{q*} is similar. ■

The term $P^{max} - P^{min}$ in the denominator validates our intuition that increasing the range of possible perturbations decreases λ^{p*}. The larger $\overline{\omega} - \underline{\omega}$ is, the larger ω can be, and thus the stronger the stabilizing term $-\omega$ is in (3b), which increases λ^{p*}. The same analysis holds for λ^{q*}.

Remark 2 *There are now two approaches to answer Problem 1 based on the controls $\underline{u}$ and $\overline{u}$. If $\lambda \leq \lambda^*$, then $\underline{u} \leq \overline{u}$ and any control in between guarantees the robust control invariance of the safe set. On the other hand, if $\lambda > \lambda^*$ we need a state-dependent control law. When the state gets too close from the upper (resp. lower) bound of its safe set, applying $\overline{u}$ (resp. $\underline{u}$) prevents safety violation. Besides, $\underline{u}$ and $\overline{u}$ can be precomputed, so that the sole real-time action of the controller is to decide which one of the controls to apply.*

1.4 Ellipsoid constraints

Let $C \succ 0$ a positive definite matrix defining a safe set for the voltage v and frequency ω of an inverter $S = \{(v,\omega) : (v,\omega)^\top C(v,\omega) \leq 1\}$.

The Nagumo theorem, says that S is invariant if $f(v,\omega) \cdot n(v,\omega) \leq 0$ at all $(v,\omega) \in \partial S$ with n the external normal vector at f the dynamics at this point

$$f(v,\omega) = \begin{pmatrix} \dot{v} \\ \dot{\omega} \end{pmatrix} = \begin{pmatrix} v^0 - v + \lambda^q(Q^0 + u^q - Q) \\ -\omega + \lambda^p(P^0 + u^p - P) \end{pmatrix}.$$

Now, we need to determine the normal to the ellipse S at the point (v,ω). By taking the gradient of the level set of the quadratic function $e : x \mapsto x^\top Cx$

$$\nabla_x e(x) = Cx = \begin{pmatrix} C_{11} & C_{12} \\ C_{12} & C_{22} \end{pmatrix} \begin{pmatrix} v \\ \omega \end{pmatrix} = \begin{pmatrix} C_{11}v + C_{12}\omega \\ C_{12}v + C_{22}\omega \end{pmatrix} = n(v,\omega).$$

Then, the Nagumo invariance condition leads to

$$\begin{aligned}
0 &\geq f(v,\omega) \cdot n(v,\omega) \\
0 &\geq \big(C_{11}v + C_{12}\omega\big)\big(-\omega + \lambda^p(P^0 + u^p - P)\big) + \big(C_{12}v + C_{22}\big)\big(v^0 - v + \lambda^q(Q^0 + u^q - Q)\big) \\
0 &\geq (C_{22} - C_{11})v\omega - C_{12}(v^2 + \omega^2) + \lambda^p(C_{11}v + C_{12}\omega)(P^0 + u^p - P) + \lambda^q(C_{12}v + C_{22}\omega)(Q^0 + u^q - Q).
\end{aligned}$$

Define $a(v,\omega) := (C_{22} - C_{11})v\omega - C_{12}(v^2 + \omega^2)$, $b(v,\omega) := \lambda^p(C_{11}v + C_{12}\omega)$ and $c(v,\omega) := \lambda^q(C_{12}v + C_{22}\omega)$. Then, we want

$$a(v,\omega) + b(v,\omega)(P^0 + u^p) + c(v,\omega)(Q^0 + u^q) \leq b(v,\omega)P + c(v,\omega)Q. \tag{13}$$

Remember that P and Q are unknown, v, ω, a, b, c, P^0 and Q^0 are known, and we want to choose u^p and u^q to enforce (13).

If $b(v,\omega) \geq 0$ and $c(v,\omega) < 0$, we have $bP_{min} \leq bP$ and $cQ_{max} \leq cQ$ with P_{min}, P_{max}, Q_{min} and Q_{max} to be determined. Then, if u^p and u^q are chosen such that $a+b(P^0+u^p)+c(Q^0+u^q) \leq bP_{min}+cQ_{max}$, then (13) holds.

Now, we need to determine bounds on P and Q that can be computed quickly and that are as close as possible by using our available information about v and θ. Let us consider the case of

$$P = v\sum_{k\in\mathcal{N}} v_k\big(G_k\cos(\theta-\theta_k)+B_k\sin(\theta-\theta_k)\big) =: v\sum_{k\in\mathcal{N}} p_k(\theta,\theta_k,v_k).$$

We want $P_{min} \leq P$. Assuming $v \geq 0$, means that we want to minimize each p_k over $\theta_k \in [\underline{\theta},\overline{\theta}]$ and $v_k \in [\underline{v},\overline{v}]$. These minimizations can all be done independently. We can assume that $\underline{\theta}$ and $\overline{\theta}$ are given. The bounds on v can be determined based on the ellipsoidal safe set S.

We know that $(\overline{v},\omega) \in \partial S$, so $C_{11}\overline{v}^2+2C_{12}\overline{v}\omega+C_{22}\omega^2 = 1$. At $\overline{v}$ the normal to S is horizontal: $n(\overline{v},\omega) = (-,0)$, i.e., $C_{12}\overline{v}+C_{22}\omega = 0$, i.e., $\omega = -\frac{C_{12}}{C_{22}}\overline{v}$. Then,

$$1 = C_{11}\overline{v}^2+2C_{12}\overline{v}\left(-\frac{C_{12}}{C_{22}}\overline{v}\right)+C_{22}\left(-\frac{C_{12}}{C_{22}}\overline{v}\right)^2 = \overline{v}^2\left(C_{11}-2\frac{C_{12}^2}{C_{22}}+\frac{C_{12}^2}{C_{22}}\right) = \overline{v}^2\frac{C_{11}C_{22}-C_{12}^2}{C_{22}}.$$

Then, $\overline{v} = \sqrt{\frac{C_{22}}{\det(C)}}$ and since $\underline{v}$ verifies the same properties, we also have $\underline{v} = -\sqrt{\frac{C_{22}}{\det(C)}}$.

Then, $\overline{p_k}(\theta) = \max\left\{p_k(\theta,\theta_k,v_k) : v_k = \pm\sqrt{\frac{C_{22}}{\det(C)}},\ \theta_k \in [\underline{\theta},\overline{\theta}]\right\}$. The optimization is done over one continuous parameter θ_k and on v_k that can take one of two values. Similarly $\underline{p_k}(\theta) = \min\left\{p_k(\theta,\theta_k,v_k) : v_k = \pm\sqrt{\frac{C_{22}}{\det(C)}},\ \theta_k \in [\underline{\theta},\overline{\theta}]\right\}$. Then, we define $P_{min}(\theta,v) := v\sum\underline{p_k}(\theta) \leq P$ if $v \geq 0$, and $P_{min}(\theta,v) := v\sum\overline{p_k}(\theta) \leq P$ if $v < 0$. Same for P_{max} and for Q.

1.5 Numerical Analysis

In this section we apply our theory to a modified microgrid model [26], and demonstrate the robust control invariance of the safe sets S_v and S_ω introduced in (6). As per the modifications in [13, 16], four inverters were placed in the network, three of those at buses 1, 4, and 5, and the fourth at bus 0 after disconnecting the utility for islanded operation.

In a microgrid, the distance between inverters is small and thus the states of neighbors are strongly coupled. To account for this physical phenomenon we introduce two constants Δ_v and Δ_ω measuring the range of allowable uncertainty of neighboring inverters such that $v_k \in [v_i-\Delta_v, v_i+\Delta_v]$ and $\omega_k \in [\omega_i-\Delta_\omega, \omega_i+\Delta_\omega]$ for $k \in \mathcal{N}_i$. For the numerical analysis we choose $\Delta_v = 0.02$p.u., which is 2% of the nominal voltage v_i^0, and $\Delta_\omega = 0.12$Hz, which is 2% of the 6Hz range of S_ω. The nominal droop coefficients of the network are $\lambda^p = 2.51$rad/s/p.u. and $\lambda^q = 0.2$p.u./p.u..

The coupling adds a constraint to the calculation of Q_i^{min} and Q_i^{max}. For instance, $Q_i^{max} = \max\ Q_i(\theta_k,v_k)$ subject to $v_i = \underline{v}$, $\theta_k \in S_\theta$, $v_k \in S_v \cap [v_i-\Delta_v, v_i+\Delta_v] = [\underline{v}, \underline{v}+\Delta_v]$ for $k \in \mathcal{N}_i$. We compute Q_2^{min}, Q_2^{max} with an SOS algorithm and we use the calculations of Proposition 1 to represent $\underline{u_2^q}$ and $\overline{u_2^q}$ on Figure 1.

As proven in Proposition 2, since 0 is in the interior of S_v, we were able to find values of λ_2^q for which safety admissible controls exist. On Figure 1, λ_2^{q*} is located at the intersection of the green dash-dot lines representing $\underline{u_2^q}(\lambda_2^q)$ and $\overline{u_2^q}(\lambda_2^q)$. Figure 2 shows that the same is true for λ_2^p. The computed values of λ^* are gathered in Table 1.

Note that for the voltage λ^{q*} ranges from 80% to 217% of the nominal λ^q depending on the inverter. For the frequency, λ^{p*} ranges from 35% to 93% of the nominal λ^p.

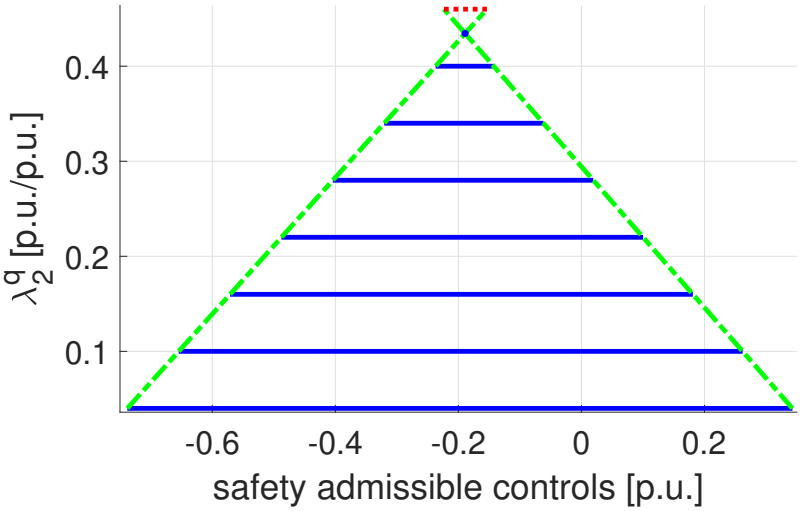

Figure 1: Evolution of the interval of safety admissible controls in blue for the voltage of node 2. The blue dot corresponds to λ_2^{q*}. The green dash-dot lines correspond to $\underline{u_2^q}(\lambda_2^q)$ and $\overline{u_2^q}(\lambda_2^q)$. The red dotted line indicates that $\underline{u_2^q} > \overline{u_2^q}$.

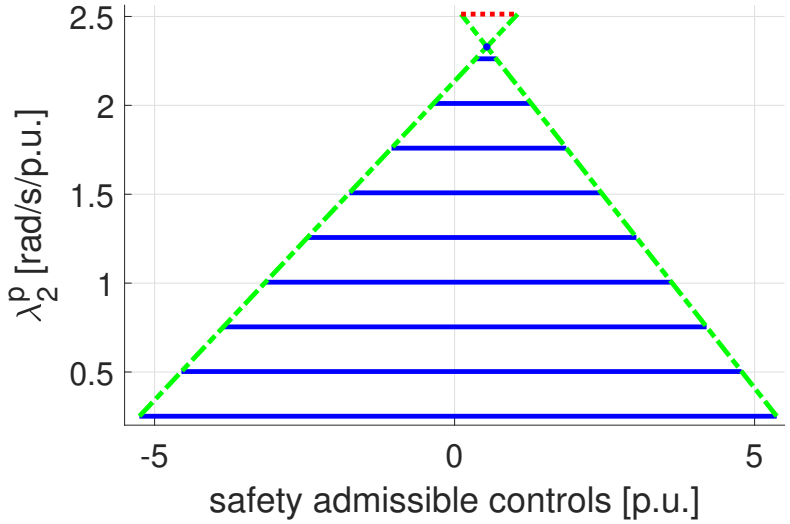

Figure 2: Evolution of the interval of safety admissible controls in blue for the frequency of node 2. The blue dot corresponds to λ_2^{p*}. The green dash-dot lines correspond to $\underline{u_2^p}(\lambda_2^p)$ and $\overline{u_2^p}(\lambda_2^p)$. The red dotted line indicates that $\underline{u_2^p} > \overline{u_2^p}$.

Inverter	1	2	3	4
λ^{p*} [rad/s/p.u.]	1.227	2.329	0.875	1.368
λ^{q*} [p.u./p.u.]	0.228	0.434	0.161	0.241

Table 1: Maximal droop coefficients λ^* for which safety admissible controls exist.

We now study how the admissible range of states Δ_v, S_θ and S_v impact the maximal droop coefficient λ^{q*}.

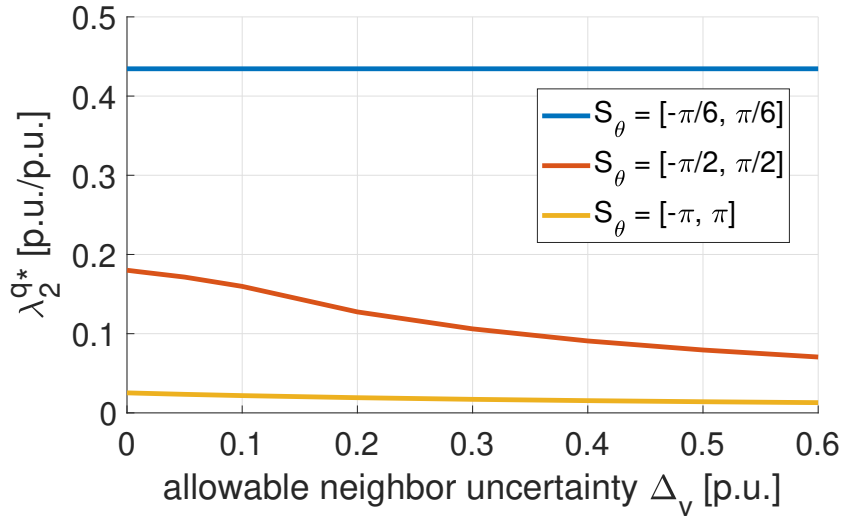

Figure 3: Evolution of λ_2^{q*} as a function of the allowable neighbor uncertainty Δ_v and of the range of admissible phase angle S_θ.

In Figures 3 and 4, $\Delta_v = 0.6$p.u. depicts a lack of coupling between inverters, because the length of S_v is at most 0.6p.u., while for $\Delta_v = 0$p.u. the coupling is perfect, i.e., $v_k = v_i$ for $k \in \mathcal{N}_i$.

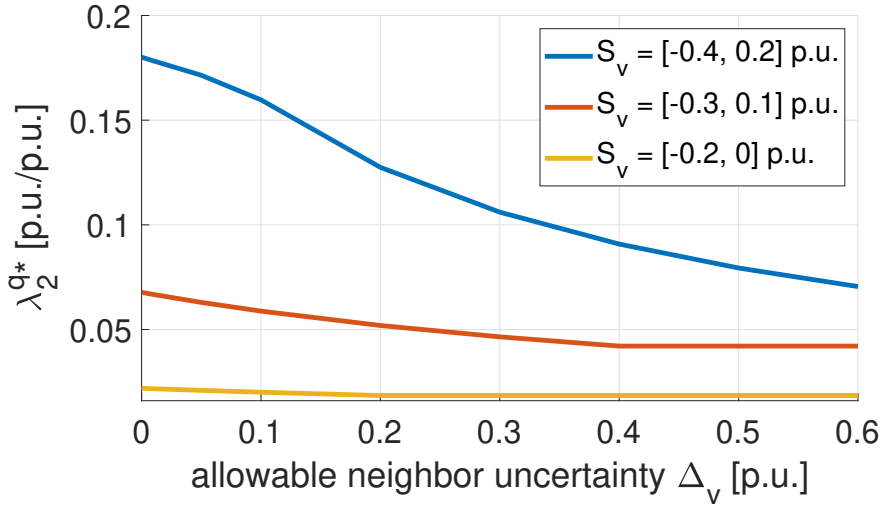

Figure 4: Evolution of λ_2^{q*} as a function of the allowable neighbor uncertainty Δ_v and of the range of admissible voltage S_v.

As predicted with (12) and illustrated on Figures 3 and 4, as the uncertainty ranges Δ_v and S_θ increase, the value of λ^{q*} decreases. The impact of the length of S_v on λ^{q*} is more difficult to predict as it affects both the numerator and denominator of λ^{q*} in (12). However, the verdict of Figure 4 is clear: enlarging S_v increases λ^{q*}, the voltage has more wiggle room inside its safe set, it is thus easier to maintain $v \in S_v$.

We compute the controls $\underline{u_1^p}$ and $\overline{u_1^p}$ on an Intel Core i7-4770S with a CPU at 3.1GHz and 8GB of RAM. Previous works [10, 13] relied on the widely used MATLAB toolbox SOSTOOLS [27] and the semi-definite programming (SDP) solver SeDuMi [28]. However, the computation times were often excessive for nodes with more than two neighbors. We thus consider the Julia language [29], its SOS toolbox [30] and the SDP solvers SDPA [31] and Mosek [32]. As expected, Julia is faster and the computation times can be reduced by two orders of magnitude as shown on Table 2.

Language	MATLAB	Julia	Julia
SDP solver	SeDuMi	SDPA	Mosek
Run-time for $\underline{u_1^p}$ and $\overline{u_1^p}$	4295s	343s	33s

Table 2: Run-time comparison between implementations.

In order to illustrate the invariance of the safe sets with the safety admissible controls calculated, we simulate the evolution of the voltage and the frequency of node 1. We use the original non-polynomial dynamics of the system. We choose λ_1^p and λ_1^q at respectively 40% and 100% of their nominal values, so that $\lambda_1^p < \lambda_1^{p*}$ and $\lambda_1^q < \lambda_1^{q*}$. Then, the intervals of safety admissible controls are $U_\omega = [-0.724, 1.571]$p.u. and $U_v = [-0.25, -0.0937]$p.u..

Every second we randomly choose a control value $u_1^q \in U_v$ and $u_1^p \in U_\omega$ as shown on Figures 5(a) and 5(b). Similarly, the states $\omega_k \in S_\omega \cap [\omega_1 - \Delta_\omega, \omega_1 + \Delta_\omega]$ and $v_k \in S_v \cap [v_1 - \Delta_v, v_1 + \Delta_v]$ of the neighboring nodes are stochastically updated every 10ms as depicted on Figures 5(c) and 5(d). The evolution of the voltage and frequency of node 1 are then pictured on Figures 5(e) and 5(f).

We can see that even randomly chosen controls, as long as they are within the safety admissible interval, enforce the safety of the system as $v_1 \in S_v$ and $\omega_1 \in S_\omega$ despite the stochastic variations of the neighbor states.

One could rightfully object that the stochastic nature of the variations of the neighbor states ω_k and v_k prevent significant changes in v_1 and ω_1 that could lead to safety violations. To overcome this limitation, we run a similar simulation where the neighbor states take their worst case values. To keep a constant phase angle $\theta_k = -\frac{\pi}{6}$rad, we need a constant frequency $\omega_k = 0$Hz and thus the frequency coupling must be removed by taking $\Delta_\omega = \infty$. We set the voltage at its lowest admissible bound, i.e., $v_k = \max\{\underline{v}, v_i - \Delta_v\}$. We keep the same stochastic controls and same values of droop coefficients.

Figure 6(a) shows how the voltage of a neighboring inverter v_3 follows its admissible lower bound. As illustrated on Figure 6(b) and 6(c) the voltage v_1 is maintained in S_v and the frequency ω_1 is maintained in S_ω despite the stochastic safety admissible controls and the lower bound neighbor states. Similar results are obtained when choosing θ_k at its upper bound $\frac{\pi}{6}$ and/or v_k at its upper bound $\min\{\overline{v}, v_i + \Delta_v\}$.

1.5.1 Network-wide Numerical Study

In this subsection, we present the time-domain simulations considering the entire network. Recall that the safety admissible controls at each inverter are still computed in a distributed manner considering the bounds on the neighbors frequencies and voltages. Note that there is no way to directly control the phase angles. They are indirectly controlled by controlling the frequencies and the phase angles are obtained by integrating the frequencies. As a result, we noticed in few simulation scenarios, the phase angles won't stay in the safe admissible range and there is a

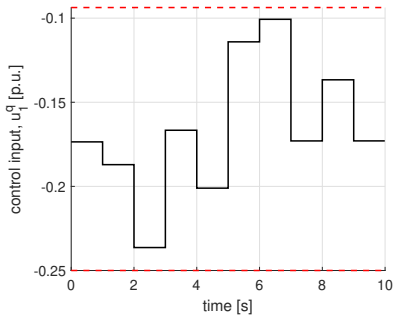

(a) Stochastic choice of $u_1^q \in U_v$, where U_v is the interval of safety admissible controls.

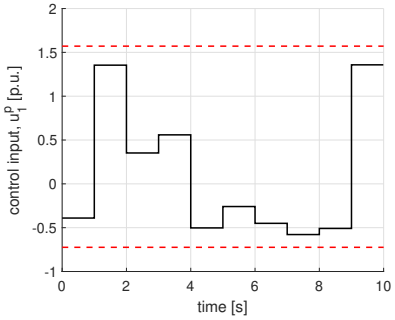

(b) Stochastic choice of $u_1^p \in U_\omega$, where U_ω is the interval of safety admissible controls.

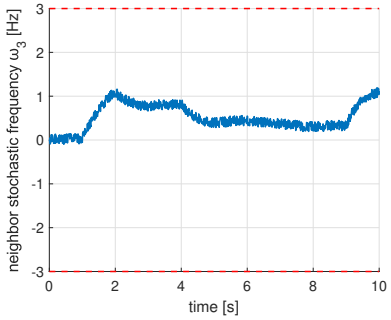

(c) Stochastic choice of neighbor frequency $\omega_3 \in S_\omega \cap [\omega_1 - \Delta_\omega, \omega_1 + \Delta_\omega]$.

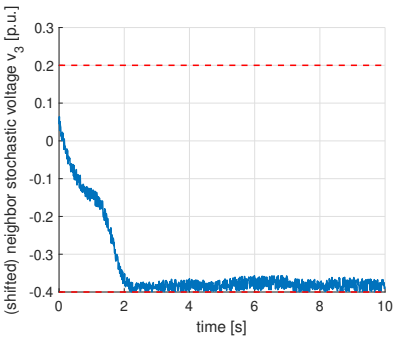

(d) Stochastic choice of neighbor voltage $v_3 \in S_v \cap [v_1 - \Delta_v, v_1 + \Delta_v]$.

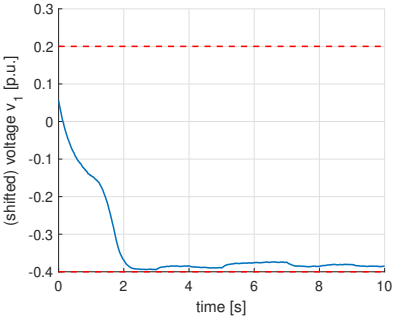

(e) Evolution of v_1, kept in S_v by u_1^q. u_1^p.

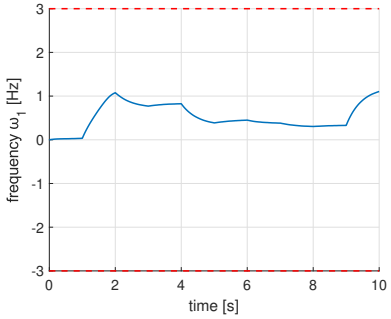

(f) Evolution of ω_1, kept in S_ω by

Figure 5: Simulation of the voltage v_1 and frequency ω_1 under stochastic safety admissible controls u_1^q and u_1^p, and stochastic variations of neighbor states θ_2, θ_3, v_2 and v_3.

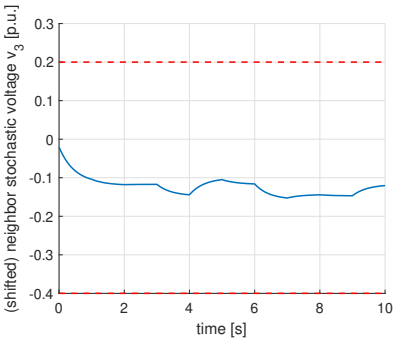

(a) Evolution of $v_3 = \max\{\underline{v}, v_i - \Delta_v\}$.

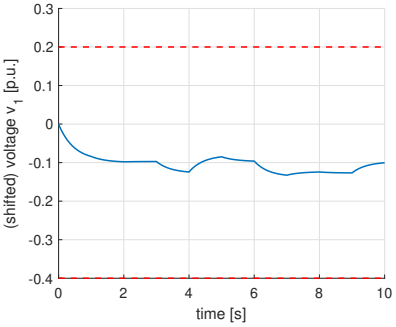

(b) Evolution of v_1, kept in S_v by u_1^q. u_1^p.

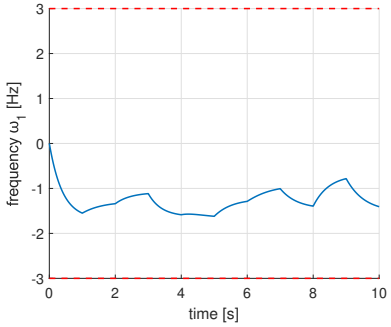

(c) Evolution of ω_1, kept in S_ω by

Figure 6: Simulation of the voltage v_1 and frequency ω_1 under stochastic safety admissible controls u_1^q and u_1^p, and lower bound choice of neighbor states θ_2, θ_3, v_2 and v_3.

need to widen the range. However, if we do so, then there is a trade-off with the maximum droop gains.

For the simulation study in Figure 7, the phase angles at each inverter is chosen to be in the range $[-\pi, \pi]$. The real and reactive power set-points to the inverters are varied every $0.1s$ and are chosen randomly in the safe admissible range as shown in Figures 7a and 7b. The corresponding phase angles, frequencies, and voltages evolve safely as shown in Figures 7c, 7d and 7e.

1.6 Further Questions

This work also raises further questions that needs to be investigated.

1. How frequently the safely admissible controls and thereby the maximal droop gains needs to be adjusted. The challenge here is the computational effort to recompute for the safely admissible controls and maximal droop coefficients.
2. The proactive local autonomy framework acts autonomously to ensure safety of the network and uses only local measurements in real-time however during the design it uses a range for the neighbor measurements. What if the local measurements are under adversarial control, then how would the proposed proactive local autonomy framework would behave needs to be studied.

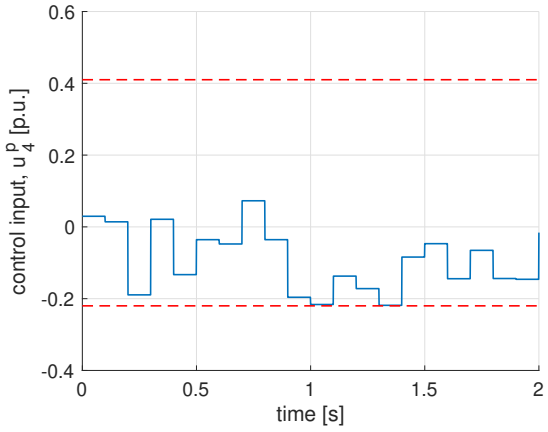

(a) Stochastic choice of $u_4^p \in U_\omega$, where U_ω is the interval of safety admissible controls.

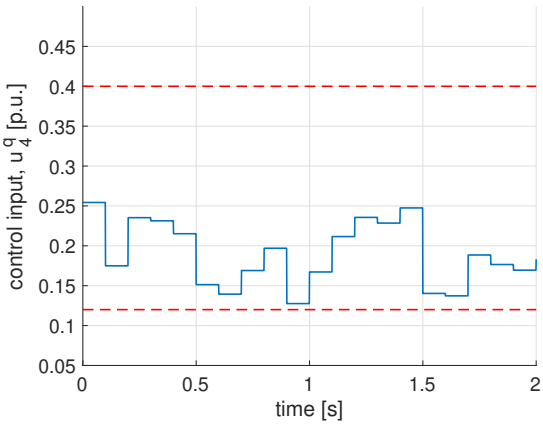

(b) Stochastic choice of $u_4^q \in U_v$, where U_v is the interval of safety admissible controls.

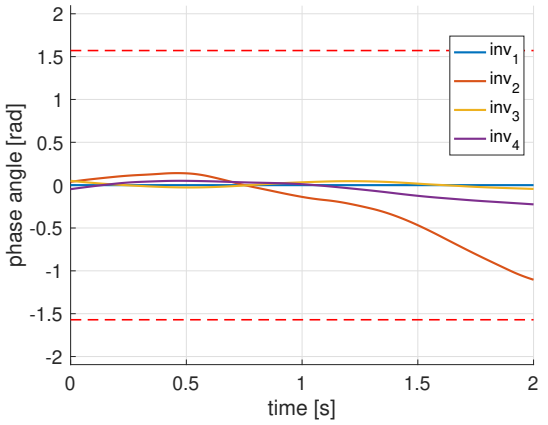

(c) Evolution of the phase angles at all inverters when subjected to a choice of safety admissible controls at each inverters.

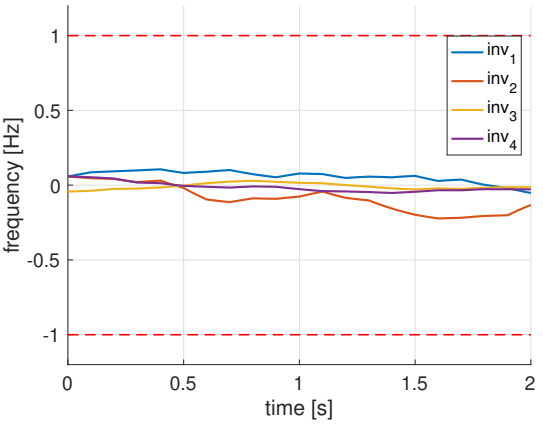

(d) Evolution of the frequencies at all inverters when subjected to a choice of safety admissible controls at each inverters.

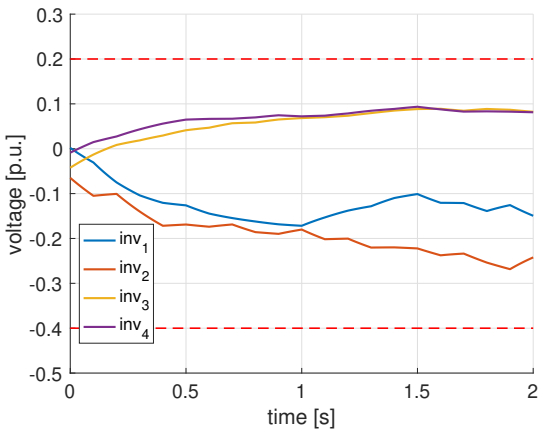

(e) Evolution of the voltages at all inverters when subjected to a choice of safety admissible controls at each inverters.

Figure 7: Simulation of the entire network for a stochastic choice of safety admissible real and reactive power inputs to the inverters.

2.0 Reactive Autonomy

Microgrids are gaining significant traction as a way to improve energy security and resilience and integrate renewable energy sources. These localized grids can operate independently (islanded mode) or connect to the main grid. At the heart of renewable-rich microgrids are inverter-based resources, playing a critical role in maintaining stability. Moreover, the distribution systems and, in particular, the microgrids are becoming more and more complex with the rapid integration of distributed energy resources, controls, communication schemes, regulatory policies, etc. [33].

Furthermore, as the cyber-physical power systems grow in complexity and size, with often different parts of the network being operated independently by different stakeholders [34], there is a strong need for advanced algorithms that allow multiple decision-making agents within the network to act autonomously to enforce resilience under different cyber-physical adversarial events.

GFMs have emerged as a key component for effectively utilizing clean and renewable energy resources in microgrids while providing stability (e.g., damping) [35]. In the hierarchy of controls for GFM inverters [36], the power-frequency droop control sits at the primary layer, adjusting the inverter (real/active) power injected into the grid to stabilize (dampen) the frequency oscillations during any disturbance. It is important to notice that the stabilized frequency needs to be at the nominal frequency, which is ensured by the secondary layer [36] operating at slower timescales and adjusting the real power reference (set-points) to the inverters across the grid.

Inverter-based resources bring forth novel challenges for the hierarchical layer of controls used to operate today's power grid [37]. One of these challenges is manifested in fast frequency dynamics, driven by low inertia and fast actions of inverter controls. As a result, there is an increasing overlap of the timescales of operation, with implications on the validity of the assumption around decoupled control layers [6], as well as on various frequency-based protections (e.g., under-frequency thresholds, rate-of-change-of-frequency) [37, 38]. Existing primary (local, device-level) and secondary (centralized/distributed, system-level) controls within the cyber-physical power systems today lack the constructive design methods to enforce operational safety limits (e.g., under- and over-frequency limits as per IEEE Standard 1547 [2]) that ensure operational resilience during transients.

Control of inverters, including GFMs, has attracted immense attention in recent years within the power and control communities. Recent research into primary (local, device-level) controls of inverters has led to novel control designs [39, 40], as well as methods for tuning controller gains for stability [10, 11]. However, the primary controls are designed and operated myopically, without any mechanism to actively enforce resilience via local measurement and control action (see [41, 42] and the references therein).

On the other hand, the secondary (centralized/distributed, system-level) control helps restore the grid's frequency to the nominal level, using various methods based on optimal control [43, 44], consensus protocols [45], passitivity [46], and blockchain-enabled controls with neural networks [47]. However, the secondary controls operate at a slower timescale and are incapable of ensuring operational resilience during transients, especially in the presence of frequent stochastic disturbances or unforeseen adversarial events. Moreover, many adversarial events in critical cyber-physical networks can propagate as a cascading failure, which often starts from local disruptions that travel through the network over a short period and can create a system-wide impact (e.g., a blackout) [48].

Some of the drawbacks of these methods include their dependency on a specific form of the inverter model and the control design is based on linearization, which significantly impacts the applicability of the controls under various operating conditions and does not enforce resilience constraints into the control design to achieve resilience irrespective of the nature of the disturbance (see [49] for a comprehensive study of merits and trade-offs of decentralized secondary controls). Moreover, most of the controls develop different secondary controls to achieve nominal

frequency and power sharing among the inverters, which also becomes a challenge as it will be difficult to finalize a secondary control strategy for real-world application.

These challenges further necessitate the need to develop agile, adaptive, and lightweight control solutions that allow the control agents to autonomously (under no communication) ensure system-wide resilience under various disturbances. Such solutions, as proposed in this work, should be

1. Minimally invasive, that is, minimal changes to the existing control architecture, so it is easy to implement and integrate with the existing control hierarchy,
2. Decentralized and autonomous (few measurements required to process controls),
3. Computationally efficient (ability to react fast), and
4. Largely model-agnostic, i.e., not tied to any specifics of the primary/device-level controls.

In this work, we develop a solution similar to the one introduced in [16] to intervene only when certain local resilience constraints are not met, and this control strategy works in tandem along an existing primary and secondary control hierarchy. We first begin by defining a safe operating region for frequency and resilience as the ability of the system to maintain this safe region irrespective of the nature of the disturbance. These controls are referred to as safety-promoting DACs, and these DACs were designed offline based on inverter nameplate details, droop gains, etc., and implemented in real-time where the inverter measurements such as the power and frequency measurements are continuously monitored and the set-points are adjusted accordingly. The DAC does not act during small disturbances and comes into play only if the frequency deviates outside the safe region. We achieve this by defining a barrier function that comes into play only when the frequencies are violating the safe limits. This work was inspired by the knowledge gained from previous works [13,16] that involved solving multiple SOS-optimization problems (which we overcome in this work and make it computationally efficient) to provide sufficient guarantees on maintaining safe region.

The main contributions of this work are described as follows:

1. Defining barrier functions for each GFM as a function of the local operational resilience constraints.
2. Developing a decentralized set-point change control strategy by applying barrier functions to local measurements to address operational resilience violations.
3. Providing sufficient guarantees on meeting the operational constraints while being agnostic to the nature of the disturbance.
4. Demonstration of the proposed decentralized control functionality under critical operating conditions in a networked microgrid system.

A key observation was the fact that the addition of the DACs results in the enhancement of the current functionality of GFMs by empowering these vital resources to act with urgency when needed. Therefore, it is important to notice that these controls complement the existing hierarchy of controls and act only when local operational resilience conditions such as frequency or voltage limits are violated.

2.1 Grid Forming Inverter Model and Inverter Controls

2.2 Grid Forming Inverter

Consider the GFM inverter with CERTS droop-controlled GFM model from [1, 50] as shown in Fig. 8. The GFM inverter model consists of a P-f droop control, Q-V droop control as well as over- and under-load mitigation strategy.

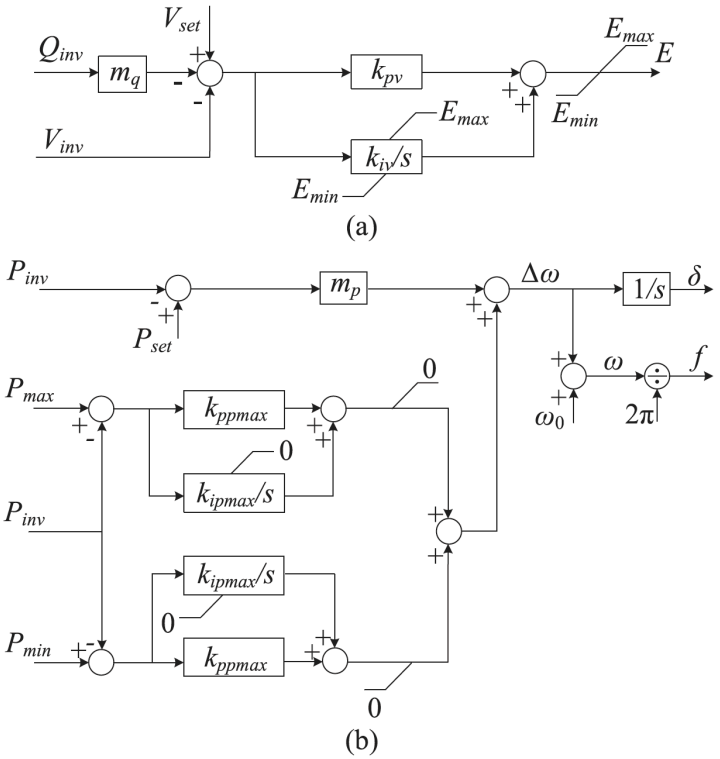

Figure 8: CERTS droop-controlled GFM inverter model, with (a) Q-V droop control, and (b) P-f droop control, including over- and under-load mitigation (adopted from [1]).

In addition, there are low-pass measurement filters that measure the active (P), reactive (Q) power, and voltage at the point of common coupling for the inverter. $P_{\text{grid},\phi}$ and $Q_{\text{grid},\phi}$ are the active and reactive power injections from the inverter into the grid, at phase $\phi \in \{a, b, c\}$ while $V_{\text{grid},\phi}$ is the voltage at phase $\phi \in \{a, b, c\}$. The inverters also honor power rating constraints; therefore,

$$P_{\text{grid}} \in [P_{\text{min}}, P_{\text{max}}]$$

With the assumption that $\dot{P}_{\text{set}} = 0$ (i.e., the P_{set} is changed slowly compared to the inverter droop control timescales), we have the P-f droop equations given by

$$\dot{\delta} = \omega - \omega_0 \tag{14}$$

$$\tau\dot{\omega} = -(\omega - \omega_0) + m_p (P_{\text{set}} - P_{\text{inv}}) \tag{15}$$

where $P_{\text{inv}} := \sum_{\phi\in\{a,b,c\}} P_{\text{grid},\phi}$, ω_0 is the nominal frequency, m_p is the P-f droop gain and P_{set} is the input to the inverter dynamics. As mentioned earlier, the P_{set} dynamics and the inverter droop control dynamics operate at different timescales, and as such there are separate control strategies for controlling the inverter dynamics (primary control) and P_{set} dynamics (secondary control) [12].

Primary Controls

The P-f droop control at the GFM inverters acts as a primary control to the inverters and operates at millisecond (ms) timescales. The P-f droop controls (based on the internal inverter measure-

ments) react quickly to any disturbance in the system to stabilize the frequency. The input to the droop controls is the reference set-point (P_{set} or Q_{set}), which is usually provided by the secondary controls. The action of the droop controls in most cases will stabilize the frequency; however, there are no guarantees that the frequency will go back to the nominal frequency (60 Hz).

Secondary Controls

The real power set-points to the inverters are updated by the secondary controls by accessing the inverter measurements. These controls could be either centralized or distributed and operate at slower timescales (in the order of a few seconds), compared to primary controls. The objective of this control is to change the real power set-points in such a way that the frequency reaches nominal with equal power sharing among the inverters. The secondary controls discussed in [45] are implemented in this work. These controls are based on the leader-follower consensus framework and coordinate the GFM and grid-following (GFL) inverters to achieve frequency restoration to nominal frequency and accurate power sharing.

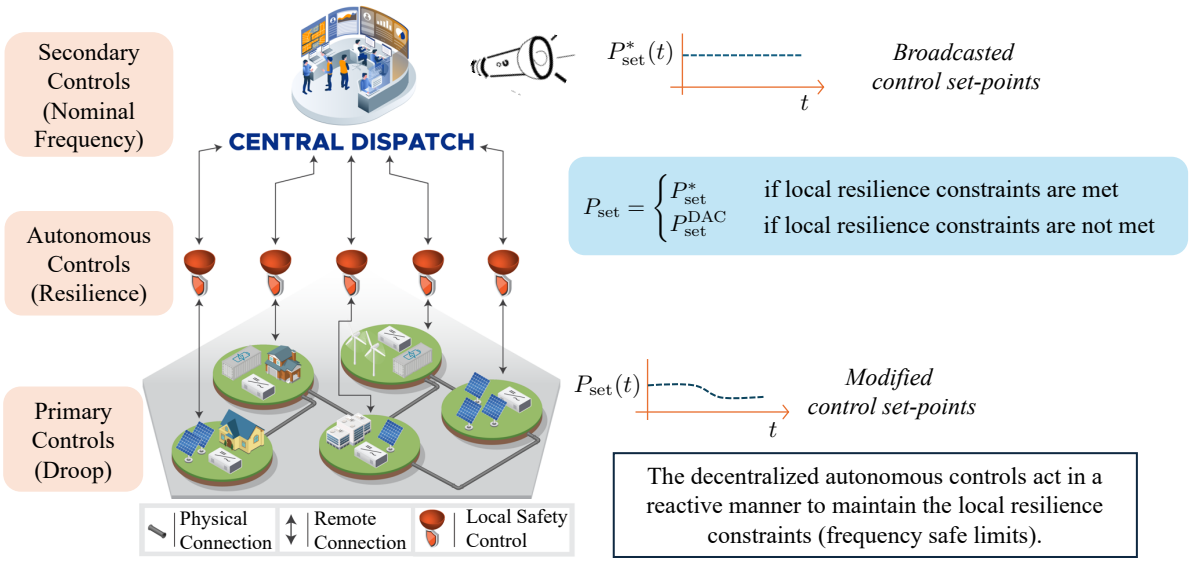

Figure 9: Overview of the functioning of the proposed DAC: These inverter-based controls are located between primary and secondary controls. When the frequency resilience constraints are violated, these controls adjust the secondary control set-points to ensure frequency resilience, otherwise, these controls will not intervene and pass the secondary control set-points to the inverter. These autonomous controls are computationally efficient and rely solely on local measurements available at the inverters themselves.

In the scope of this work, we define a safe operating region around the nominal frequency and define resilience as the ability of the system to maintain this safe region irrespective of the type of events happening on the system. Considering the timescale gap between the primary controls and secondary controls of operation there is a blind spot and if an event happens during this period the primary controls react but cannot ensure frequency resilience that could avoid any violations that lead to blackouts. To bridge the timescale gap between the primary and secondary controls and achieve resilience, we introduce reactive controls that are decentralized and maintain resilience.

The functioning of the DACs is illustrated in Fig. 9 and is described in detail in the following section.

2.3 Decentralized Autonomous Controls

In this section, we present a decentralized autonomous control framework that utilizes a few local measurements from the inverters to maintain a predefined safe region for frequency under disturbances. We begin by defining the local resilience constraints at each inverter.

At each inverter, suppose the frequency limits are defined as $\omega \in [\omega_{\text{min}}, \omega_{\text{max}}]$ where $\omega_{\text{min}}, \omega_{\text{max}}$ are the lower and upper-frequency limits respectively. These pre-defined safe limits for frequency at each inverter form the local resilience constraints that need to be maintained irrespective of the nature of the disturbance. Therefore, the goal is to modify the set points P_{set}, such that the local resilience constraints are respected. To this end, we introduce two barrier functions, corresponding to lower and upper frequency limits, that act when frequencies deviate from the safe limits either from below or above.

Consider the following barrier functions defined as,

$$B_{\text{min}}(\omega) = \omega - \omega_{\text{min}}, \text{ such that } \begin{cases} \geq 0, & \text{Safe} \\ < 0, & \text{Unsafe} \end{cases} \tag{16}$$

$$B_{\text{max}}(\omega) = \omega - \omega_{\text{max}}, \text{ such that } \begin{cases} \leq 0, & \text{Safe} \\ > 0, & \text{Unsafe} \end{cases} \tag{17}$$

We refer to B_{min} and B_{max} as the lower and upper barrier functions respectively. When the lower (upper) barrier function is positive (negative), the lower (upper) frequency safe limit is not violated. However, in the presence of a disturbance, if the lower frequency limit is violated, we want the derivative of the lower barrier function to change its sign and become non-decreasing. Similarly, due to a disturbance, if the upper frequency limit is violated, we want the derivative of the upper barrier function to change its sign and become non-increasing. Thus we need the following conditions on the time-derivative of the barrier functions.

$$\dot{B}_{\text{min}} \geq -\alpha B_{\text{min}}^{q}, \tag{18}$$

$$\dot{B}_{\text{max}} \leq -\alpha B_{\text{max}}^{q}, \tag{19}$$

where q is required to be an odd number to preserve the sign of the right hand side of Eqs. (18)-(19) and α can be considered as control performance gain. The addition of the term, $-\alpha B_{\text{min}}^{q}$ ($-\alpha B_{\text{max}}^{q}$) on the right side of the barrier function derivative requires explanation. Whenever the frequencies are inside the safe region, the lower barrier function is nonnegative and we can allow the lower barrier function to decrease if the operating frequency is well inside the safe region. However, when the operating frequency goes outside the safe region from below, we want the lower barrier function to increase and the corresponding time-derivative to be non-negative (that is, $\dot{B}_{\text{min}} \geq 0$).

Similarly, the non-positive values of the upper barrier function indicate the frequency is within the safety limits, and the upper barrier function can increase inside the safe region as long as the operating frequency is lower than ω_{max}. However, when the operating frequency increases beyond, ω_{max}, the upper barrier function should decrease and the corresponding time-derivative should be non-positive (that is, $\dot{B}_{\text{max}} \leq 0$).

When the frequencies deviate outside the safe region due to an event, it is expected to steer the system to the safe region in finite time and to achieve this, we modify, $\dot{B}_{\text{min}} \geq 0$ to

$\dot{B}_{\text{min}} \geq -\alpha B_{\text{min}}^q$ and similarly, $\dot{B}_{\text{max}} \leq 0$ to $\dot{B}_{\text{max}} \leq -\alpha B_{\text{max}}^q$. To achieve the desired performance to maintain safety while ensuring the smoothness of the resulting control adjustment, we chose $q = 3$. Therefore, from Eq. (18), we have,

$$\begin{aligned} P_{\text{set}} &\geq P_{\text{inv}} + \frac{1}{m_p}\left(\omega - \omega_0 - \alpha(\omega - \omega_{\text{min}})^3\right) \\ \implies \omega &\geq \omega_{\text{min}} \quad \text{(lower limit)} \end{aligned} \tag{20}$$

Similarly, from Eq. (19), we have,

$$\begin{aligned} P_{\text{set}} &\leq P_{\text{inv}} + \frac{1}{m_p}\left(\omega - \omega_0 - \alpha(\omega - \omega_{\text{max}})^3\right) \\ \implies \omega &\leq \omega_{\text{max}} \quad \text{(upper limit)} \end{aligned} \tag{21}$$

The set-point changes suggested by Eq. (20) and Eq. (21) result in a frequency that is within the safe region. However, as the scope of this work is only concerned with maintaining the safe region and allowing the secondary control to drive the frequency to the nominal value, it is sufficient to make minimal set-point changes such that either $\omega = \omega_{\text{min}}$ or $\omega = \omega_{\text{max}}$ is maintained. This results in the following conditions.

$$\begin{aligned} P_{\text{set}}^{\text{low}} &= P_{\text{inv}} + \frac{1}{m_p}\left(\omega - \omega_0 - \alpha(\omega - \omega_{\text{min}})^3\right) \\ &\implies \omega = \omega_{\text{min}} \end{aligned} \tag{22}$$

$$\begin{aligned} P_{\text{set}}^{\text{up}} &= P_{\text{inv}} + \frac{1}{m_p}\left(\omega - \omega_0 - \alpha(\omega - \omega_{\text{max}})^3\right) \\ &\implies \omega = \omega_{\text{max}} \end{aligned} \tag{23}$$

When any event on the system drives the frequencies outside the safe region either from below (under frequency event) or above (over frequency event), the set-points to the GFM inverters are adjusted accordingly either by Eq. (22) or Eq. (23) to maintain the safe region.

These two cases are combined to deploy these safety controls at the inverters. Let P_{set}^* be the set point given by the secondary controls or central dispatch to the inverter and let P_{set} be the set-point seen by the inverter. Since the safe controls always act to maintain the safe region, we have,

$$P_{\text{set}} = \begin{cases} P_{\text{set}}^* & \text{if } \omega_{\text{min}} \leq \omega \leq \omega_{\text{max}} \\ P_{\text{set}}^{\text{DAC}} & \text{otherwise} \end{cases} \tag{24}$$

where

$$P_{\text{set}}^{\text{DAC}} = min(P_{\text{set}}^{\text{up}}, max(P_{\text{set}}^{\text{low}}, P_{\text{set}}^*)) \tag{25}$$

where $P_{\text{set}}^{\text{DAC}}$ denotes the set-points that are modified by the safety-promoting DACs. Note that the control performance gain α is chosen in such a way that these safety-promoting DACs won't act if frequency violations will not happen. Therefore, when $\omega_{\text{min}} \leq \omega \leq \omega_{\text{max}}$, $P_{\text{set}} = P_{\text{set}}^*$, which essentially indicates that the real power set-point provided by secondary controls will be passed to the inverter. Furthermore, the following criterion ensures that the DACs set-point changes respect the capacity constraints, we have the following criterion.

$$\begin{aligned} P_{\text{set}}^{\text{max}} &= \sqrt{S_{\text{inv}}^2 - Q_{\text{inv}}^2} \\ P_{\text{set}} &= min(P_{\text{set}}^{\text{max}}, max(P_{\text{set}}^{\text{min}}, P_{\text{set}})), \end{aligned} \tag{26}$$

where $Q_{\text{inv}} = \sum_{\phi \in \{a,b,c\}} Q_{\text{grid},\phi}$, and S_{inv} is the size of the inverter. The implementation of the safety-promoting DACs is illustrated in Fig. 10. The DACs use only a few measurements from the inverters to adjust the real power set-points at the inverters and maintain the safe frequency region (in other words, local resilience). The real power control set-points are modified according to Eq. (25) which is an algebraic equation, and as a consequence, these controls are computationally efficient. Therefore, due to the decentralized autonomous and computationally efficient properties of the DACs, they are more suitable for real-world applications.

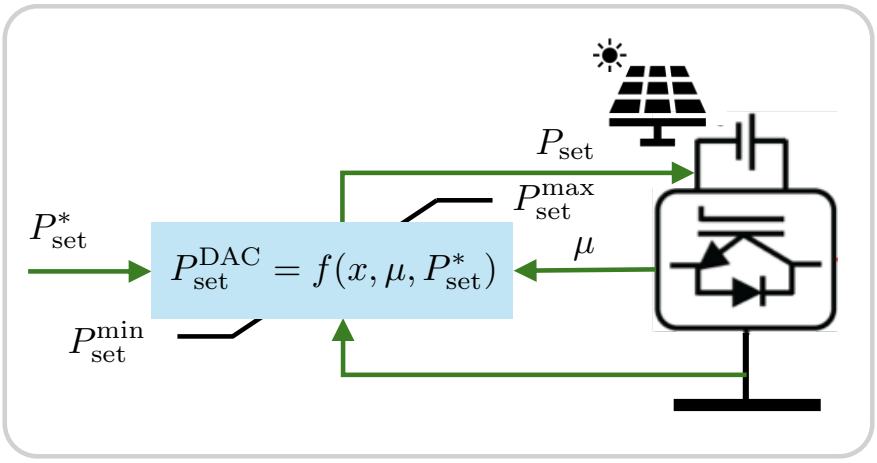

Figure 10: DAC implementation at each inverter. P_{set}^{*} denotes the set-point sent by the secondary control, $\mu = (S_{\text{inv}}, m_p)$ denotes the fixed parameters at the inverters and $x = (\omega, P_{\text{inv}}, Q_{\text{inv}})$ denote the measurements from the inverter.

Fig. 11 provides an overview of how the DACs function during the onset of a dynamic event. When a dynamic event occurs that results in an over-frequency event and the safe region is violated, the control set-points are modified in such a way that the frequency safe region is maintained (that is, $P_{\text{set}}^{\text{DAC}}$ modified such that $\dot{B}_{\max} \leq 0$).

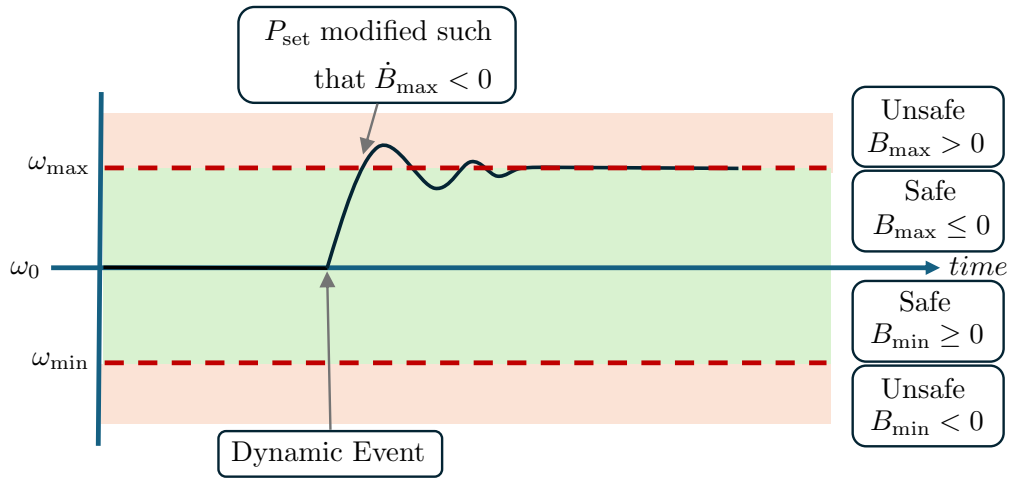

Figure 11: Illustration of the functioning of safety promoting DACs when frequency violations occur.

The following algorithmic procedure encapsulates the entire DAC implementation methodology

applicable to any GFM inverter.

Algorithm 1 DAC algorithm to compute the new set-point at any GFM inverter

Require: Fixed parameters $S_{\text{inv}}, m_p, \alpha$

Inputs: $\omega, P_{\text{inv}}, Q_{\text{inv}}, P^*_{\text{set}}$

Compute $P^{\text{low}}_{\text{set}}, P^{\text{up}}_{\text{set}}$ from Eqs. (9)-(10)

Find P_{set} from Eq. (11).

Use Eq. (13) to ensure P_{set} is within the absolute limits.

Outputs: P_{set}

2.4 Control Performance Design Guidelines

The control performance parameters, α and q are introduced to ensure certain conditions on the time-derivative of the barrier functions which results in appropriate control setpoint changes to guarantee the safe frequency region. Since we want the control to act minimally inside the safe bounds and act significantly when outside the safe region, we cannot have a constant rate of change for the derivatives of B_{min} and B_{max}, and hence the derivatives of B_{min} and B_{max} need to be nonlinear as a function of the frequency deviation. This is achieved by introducing q and theoretically, q can be any odd natural number.

However, for large q, B^q_{min} or B^q_{max} grows exponentially fast for large deviations in frequency and makes the control extremely aggressive. Thus, for practical consideration, we cannot choose large q. Therefore, for large deviations in ω, $\dot{B}_{min}$ and $\dot{B}_{max}$ becomes extremely large. On the other end, for $q = 1$, the derivatives of the barrier function remain constant both inside and outside the safe region. Hence, we chose $q = 3$, the smallest odd natural number greater than one.

To control the time-derivative of barrier functions, the control performance gain, $\alpha > 0$ is introduced in Eqs. (18)-(19). For a given $\alpha > 0$, B_{min} or B_{max} reaches steady state exponentially. In practical scenarios, the value α is adjusted to magnify the frequency error, thereby enabling smoother control. Consequently, the selection of α depends on the chosen value of q. For instance, consider $q = 3$, $\omega_{\text{min}} = 59.5Hz$, $\omega_{\text{max}} = 60.5Hz$ and current $\omega = 59.4Hz$. Then α must be at least $|(59.4 - 59.5)^3| = 0.001$. If $\alpha \leq 0.001$, then the control does not see any deviation from the safe region and hence won't act. However, suppose if $\alpha > 0.001$, then the controls would start acting and the control action becomes aggressive if α is larger.

The following section demonstrates the use of DACs to empower the grid operation and ensure resilience under various operating conditions.

2.5 Demonstration of the DAC Functionality Under Various System Operating Conditions

This section details how the DACs are integrated with the grid simulations through the control-grid co-simulations. Fig. 12 shows the main components of the control-grid co-simulation framework (for details we refer the reader to [51, 52]). In the following, we discuss the various operating conditions of the system considered and present the simulation results while demonstrating the versatility of the proposed DAC.

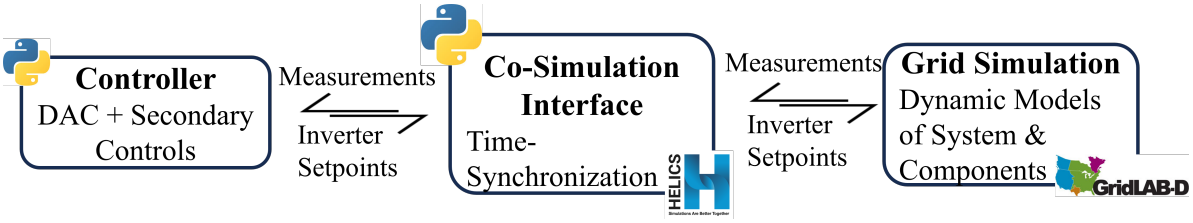

Figure 12: Control-grid co-simulation framework used for the simulation study.

2.6 IEEE 123-node System Model

The authors in [53] considered the standard IEEE 123-node test system and modified it to form four independent regions of which 3 can be formed as microgrids using diesel generators (DGs) and GFLs. The redesigned system features three independent, self-regulating microgrids alongside a PV-rich zone reliant on external support for stable operation. This results in three microgrids and a *dependent region (Region 4)* that cannot function as a standalone microgrid. In this manuscript, by starting with the modified IEEE 123-node test system developed in [53], we convert some of the GFLs to GFMs to demonstrate the uniqueness of the proposed DAC. The various use cases in the case studies focus on Microgrids 2 and 3 working together to power Region 4, leveraging its abundant solar energy as part of the black start assist/ Region 4 re-energizing use case. These inverters do not actively regulate voltage or frequency, but the PID control does act to maintain maximum active power output. Furthermore, all the GFL inverters are compliant with IEEE 1547-2018 standards.

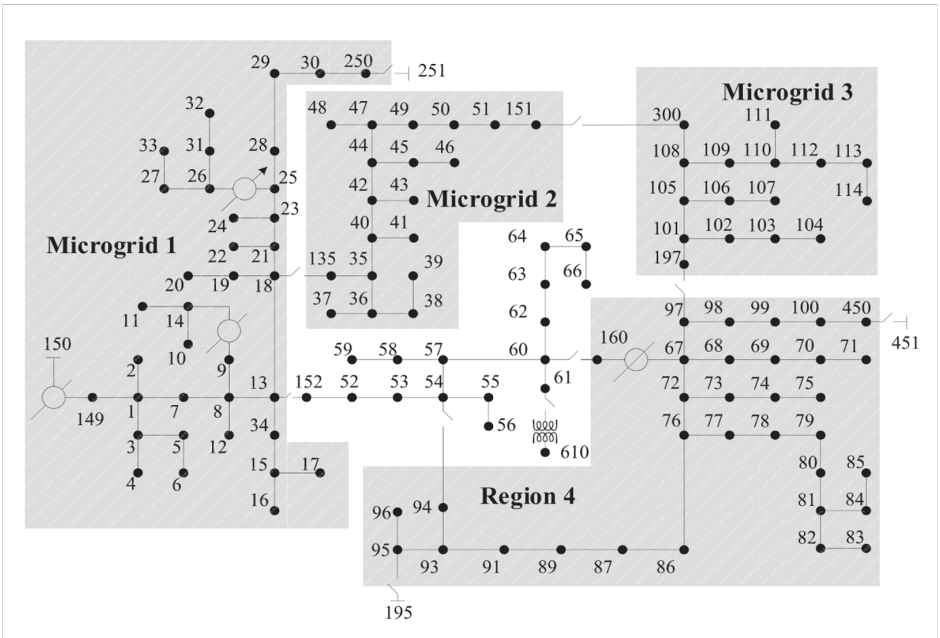

Figure 13: Illustration of the IEEE 123-node system identifying the 4 regions of the microgrids.

For the various case studies detailed below, there are small modifications done to the resources in terms of the number of DGs, GFMs and GFLs and their corresponding capacities to demonstrate specific unique functionalities of the developed controls under some limiting scenar-

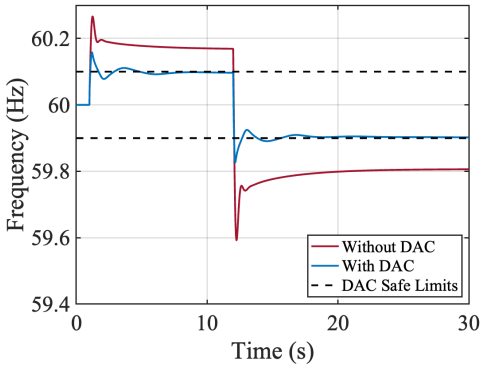

(a) System frequency in Microgrids 2 & 3

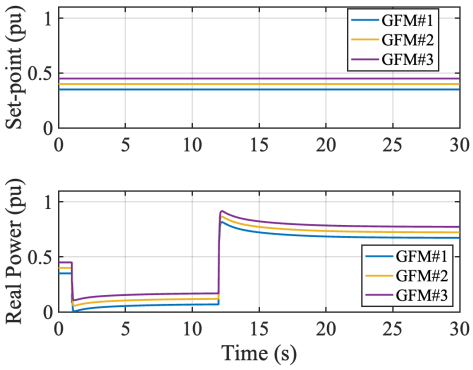

(b) Inverter set-points & power outputs without DAC

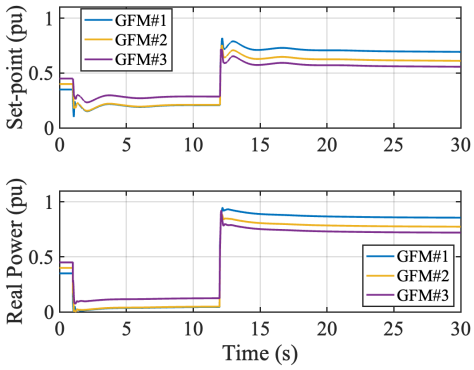

(c) Inverter set-points & power outputs with DAC

Figure 14: Results demonstrating the performance of DAC and its importance in maintaining the safe operation of the system.

ios. We will focus on Microgrid 2 and 3 resources along with resources in Region 4.

2.7 Performance of DAC During System Transients

To demonstrate the performance of the DAC during system transients, a simulation study was performed with the test system described above. The subsystems studied were Migrogrids 2 and 3 along with Region 4. The resources in these regions consist of two DGs (total capacity of 2 MVA), three GFMs (total capacity of 1.3 MVA), and two GFLs (total capacity of 220 kVA). Three GFM inverters were used to demonstrate the functionality of DAC using more controllable resources.

From the simulation results, it is clear that with just the droop controls, there is no assurance that the frequency will be within the pre-defined safe limits. However, with DAC, it was observed that the safe limits are maintained ensuring local resilience. Fig. 14 shows the frequency response and inverter outputs for the dynamic event with and without DAC. The microgrids are formed at $t = 1s$ such that Region 4 is disconnected and Microgrids 2 and 3 operate together. The generation-load imbalance causes the frequency to increase as a result of reduced load for the generation resources. At $t = 12s$, Region 4 is connected to Microgrid 3. At this instant,

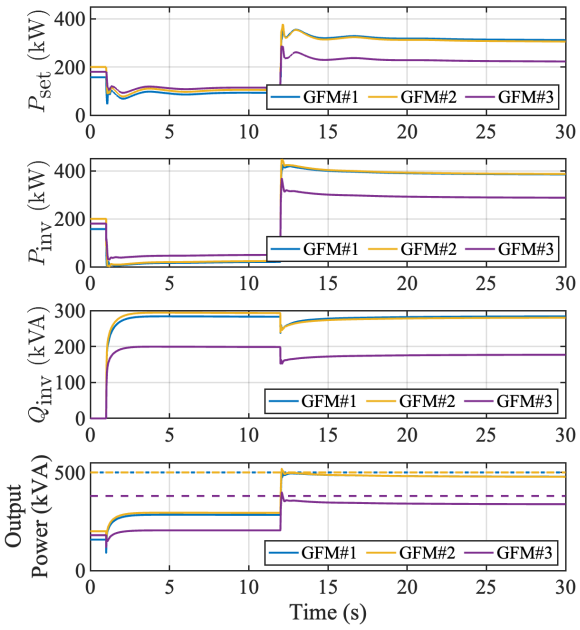

Figure 15: Real power set-point, real, reactive, and apparent powers at all the 3 GFMs. The dotted line in the bottom plot indicates the inverter size (S_{inv}).

the connection of Region 4 creates a large transient that increases the load on the generation resources, causing the frequency to dip. The GFM inverters always have their droop controls active. The safe frequency limit for this case was chosen to be 59.9 Hz to 60.1 Hz.

2.7.1 Results without DAC

For the case without DAC, when the microgrids are formed at $t = 1s$ as a result of islanding, the droop controls activate and reach a steady state with the frequency settling above the (upper) safe limit. It can be seen from Fig. 14(b) shows that there is no change in the set-points of the GFM inverters. The outputs from the inverters are reduced due to droop controls. At $t = 12s$, when the Region 4 is connected, a large amount of load gets connected to the system (Microgrids 2 and 3). This results in a frequency dip and the droop controls push the GFM outputs to increase causing the frequency dip to eventually settle to about 59.8 Hz, which is lower than the lower limit of the safe limits.

2.7.2 Results with DAC

In the case of activating the DACs, the droop control functionality is enhanced, which will utilize the GFM inverters to try and maintain the system frequency within the safe limits. The results in Fig. 14(a) show that the system frequency in microgrids 2 and 3 are maintained within the safe limits for both the transients at $t = 1s$ and $t = 12s$. In both these transients, the developed DAC reacts immediately once the frequency violates the safe limits and adjusts the inverter set-points to ensure frequency resilience. Fig. 14(c) shows the inverter set-points and inverter outputs that honor the set-points to ensure the system frequency does not go beyond the safe limits.

It is important to note that the presence of DAC arrests the frequency overshoot and the frequency NADIR is much closer to the safe limit during both events. This demonstrates that, by modifying the set-points accordingly, the DAC ensures the effective utilization of available resources to maintain local resilience.

2.8 Impact of DAC on System Performance under a Large Disturbance

The DAC can prove vital when the system experiences large disturbances as they were able to guide the traditional primary (droop) controls by modifying the set-points accordingly to steer the system away from eventual instability. One such limiting scenario is considered in this subsection.

For this scenario simulation, in the region of interest, the resource mix in the test case consists of three DGs, one GFM inverters, and three GFL inverters. The GFL inverters in the system comply with IEEE std. $1547-2018$ fault ride through (FRT) requirements and have the FRT relays set up to trip them in the must-trip zones [2].

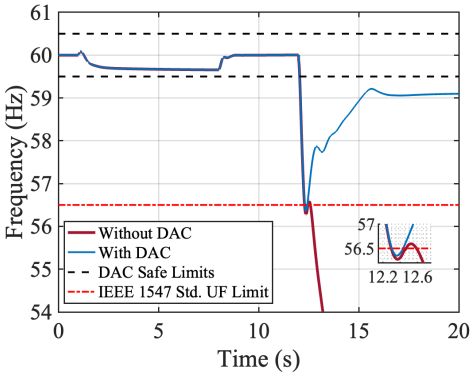

(a) System frequency in Microgrids 2 & 3

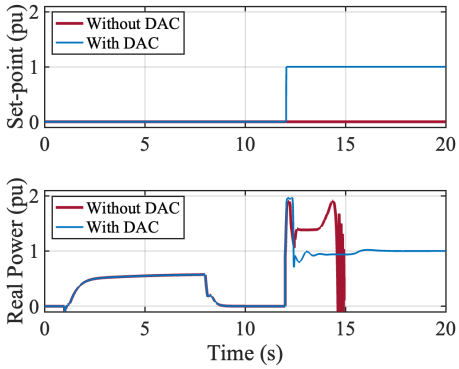

(b) GFM inverter set-points and power output with and without DAC

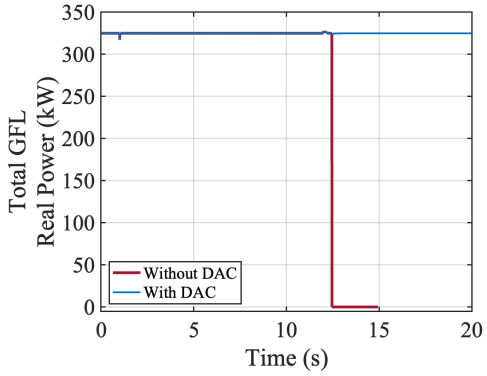

(c) Total GFL inverter output for the cases with and without DAC

Figure 16: Re-energization of Region 4 at $12s$ without DACs results in tripping of all three GFL inverters according to the IEEE 1547 standard [2].

Microgrids 2 and 3 work together to energize Region 4, by leveraging its abundant solar energy as a part of black start assist. Both the microgrids are operating at nearly maximum solar power

output, with DGs providing an additional 997 kVA of backup. The GFM inverter in Region 3 (GFM#2) is modeled as a reserve resource rated 75 kVA. The Region 4 load is 920 kVA, which means there is resource adequacy from a capacity perspective to energize Region 4. However, the case study reveals additional resource utilization to handle the dynamics of the switching transient when the Region 4 is connected.

The black start assist use case is simulated to demonstrate the performance of the proposed DACs under the described extreme switching transient. The simulation setup includes islanding the networked microgrids discussed in the previous subsection IV-A at $t = 2s$ to form microgrids in Regions 2, 3 and 4. At $8s$, the DGs are re-dispatched to bring the frequency of microgrids 2 and 3 to the nominal 60 Hz. The GFM inverter is equipped with the traditional GFM droop controls that help respond to voltage and frequency changes in the system. The re-energization of Region 4 is attempted at $t = 12s$.

The simulations are performed with and without DAC to compare the DAC functionality for overall system performance improvement. Fig.16(a) shows the frequency safe limits and the IEEE $1547 - 2018$ FRT threshold for GFL to trip if the system frequency goes below 56.5 Hz for 160 ms [2]. Fig.16(b) shows the inverter set-points and GFM inverter outputs and Fig. 16(c) shows the combined GFL inverter outputs.

2.8.1 Results without DAC

For this simulation without DAC, the frequency response of the system from Fig. 16(a) shows that the frequency excursion after the Region 4 connection at $t = 12s$ lasts long enough to trip the GFL inverters after riding through the fault as per the IEEE 1547 FRT guidelines [2]. Fig. 16(c) shows that the output powers of GFL inverters drop to zero as a result of tripping of the GFL inverters. The tripping of the GFL inverters results in a significant reduction in generation in the system, which eventually results in the collapse of the entire system of networked microgrids. Fig. 16(b) shows how the GFM inverter struggles to keep up after the GFL inverters trip, and eventually has very large power oscillations just before the system collapses and simulation blows up.

2.8.2 Results with DAC

The co-simulation with DAC results in a stable system operation. The system's responses and results of co-simulation are also seen in Fig. 16. When the frequency excursion goes beyond the safe region, the developed DAC attempts to bring the frequency within the safe limits (Fig. 16(a)). In this case, the frequency excursion is well beyond the safe limits, which makes the DAC issue the real power set-point to the GFM inverter, $P_{\text{set}} = 1$. This overrides the inverter's default droop controls, which would make the inverter respond slower without the DAC. However, with DAC, as the GFM inverter starts responding sooner with its maximum output, the frequency NADIR is minimally improved and can be seen in Fig. 16(a). This fast response of the GFM inverter due to DAC helps to improve the frequency response, and in this case, just sufficient to prevent the GFL inverters from tripping. Fig. 16(c) shows that the GFL inverters do not trip in the presence of DAC.

In this scenario of Region 4 re-energization, maintaining system operation with DAC is encouraging. To further understand the role of these controls and quantify the advantages of using DAC, we repeated the simulations by considering a range of inverter (GFM#1) sizes and compared them against the case without DACs. Fig. 17 shows how, as a function of the change in the inverter size, the violation time changes. The violation time indicates how long the frequencies were below the 56.5 Hz threshold. Clearly, with smaller inverter sizes below, 62 kW, even in the presence of DAC, when Region 4 is re-energized, the combined system cannot manage the

power generation and demand resulting in an unstable system. On the other side, for inverter size above 73 kW, even the droop controls (without DAC) stabilize the system when Region 4 is connected. This shows that with the DAC, working with an inverter whose size is nearly 15% will maintain the same violation time. From a different perspective, while keeping the inverter size the same, with DAC, we could achieve a 21% reduction in the violation time compared to without DAC thereby enhancing the robustness of the system performance. This demonstrates again the efficient utilization of available resources by DACs to maintain stability and empower the grid under various operating conditions.

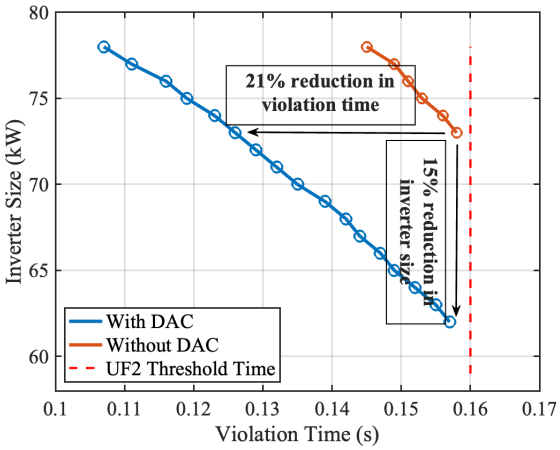

Figure 17: Impact of DACs: With DACs at inverters, one could operate with less inverter size to achieve similar performance or achieve robustness while working with the same inverter size.

2.9 Cyber-Attack Resilience with DAC

The system under consideration was modified slightly to demonstrate the cyber-attack resilience of the DAC. The regions of interest are Microgrids 2 & 3 along with Region 4. The resources in these regions consist of two DGs (total capacity of 2 MVA), three GFMs (total capacity of 1.3 MVA) and two GFLs (total capacity 220 kVA) like in the case of Section 2.5-B. The number of GFM inverters is made three to demonstrate the impact of cyber-attacks on some GFM inverter power set-points and its impact on the system performance with and without DAC. The dispatch to the microgrids is controlled by a secondary control algorithm that is described in [45].

Since the DACs use local measurements, they can prevent any malicious secondary control signals that can result in the system frequency going beyond the safe limits. Most of the GFM primary controls like droop controls cannot perform this action and will usually directly honor the secondary control dispatch. Fig. 18 shows the results of the two cases with and without DAC that demonstrate the attack resilience that comes with the proposed DAC.

The nature of the cyber-attack is described as follows. The pre-disturbance set-points are treated by the attacker as nominal set-points and during the attack window, the attacker simply masks the actual secondary control setpoints provided to the inverters and instead sends the nominal set-points irrespective of the underlying disturbance on the system. As a result of this, depending on the type of disturbance the system is undergoing, the impact on the system will be different.

In Fig. 18, the results show that in the absence of DAC, during the cyber-attack from $t = 2s$ to $t = 16s$, the GFM inverter set-points are impacted. The case study is focused on bringing out

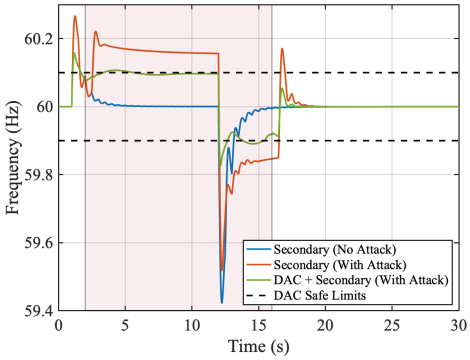

(a) Frequency in Microgrid 2 & 3

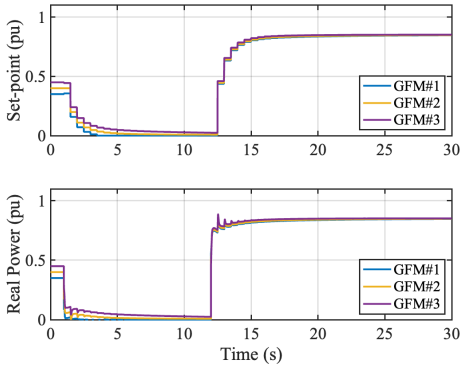

(b) GFM inverter set-points and power outputs for the case with no cyber-attack

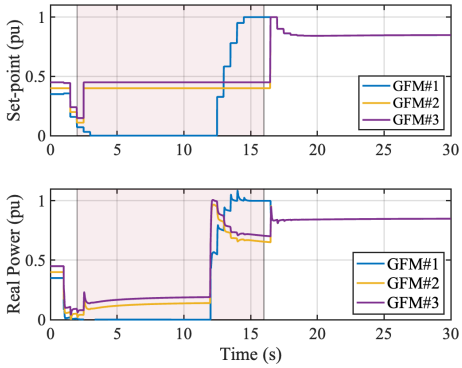

(c) GFM inverter set-points and power outputs for case with only secondary controls during cyber-attack

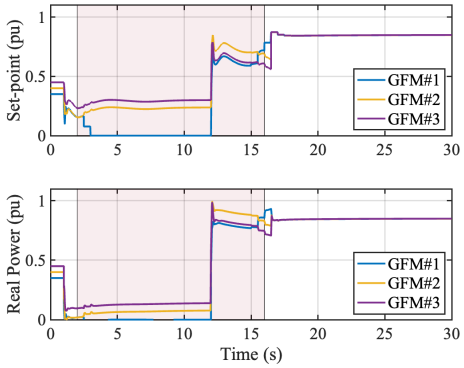

(d) GFM inverter set-points and power outputs for case with DAC and secondary controls during cyber-attack

Figure 18: Simulation results showing the cyber-attack resilience provided by the developed DAC (cyber attack duration is from $t = 2s$ to $t = 16s$). The Microgrids 2 & 3 are formed at $t = 1s$, and Region 4 is energized at $t = 12s$.

the capability of the DAC due to the use of local measurements but is not focused on the details and modality of the cyber-attack. The inverter set-point modification emulates a cyber-attack to change the power outputs of the GFM inverters. In this scenario, GFM#2 and GFM#3 are attacked and GFM#1 inverter set-points are not attacked. This allows us to visualize how the system components respond individually in the presence and absence of cyber-attacks. All the cases described below have GFM droop controls active.

The "Secondary (No Attack)" response in Fig. 18(a) and Fig. 18(b) show the results for a case of deployment of the secondary controls under no cyber-attack scenario. This case is that of an ideal operating condition where the GFM droop controls with the secondary controls from [45] can maneuver the system to achieve a stable 60 Hz (nominal frequency) operation. However, these controls cannot function as expected during an attack on them, and as a result, they are not capable of ensuring that the frequency goes back to nominal or maintains the safe region. The next subsections discuss the results with and without DAC to demonstrate the versatility of the developed DAC that can alleviate the impact of a cyber-attack.

2.9.1 Results without DAC

The results show that in the absence of DAC, the GFM inverter outputs vary as per the secondary control set-points irrespective of the safe limits. It is important to note that the inverters have the default droop controls as their primary controls are active throughout the simulation. As the inverter responds to set-point increase (due to the cyber-attack) as shown in Fig. 18(c), the frequency in the system increases to go beyond the safe limit during $t = 2s$ to $t = 12s$ (Secondary (With Attack) case in Fig. 18(a)). The key functionality of the secondary controls is to maintain the nominal frequency of 60 Hz, however, due to the compromised set-points, the frequency is not 60 Hz and goes beyond the safe limits as well. It is also interesting to see that the GFM#1 inverter's output powers go to $P_{\text{set}} = 0pu$ trying to bring down the frequency between $t = 2s$ to $t = 12s$. The GFM inverter cannot lower its power output any further in this operating scenario.

At $t = 12s$, the system undergoes the Region 4 re-energizing transient, where the frequency drops, but the GFM#2 and GFM#3 inverters do not change the power outputs as the set-points were under attack until $t = 16s$, and with the incorrect/inappropriate set-points from the secondary controls, these inverters fail to modulate the power output in response to the transient. This results in a frequency dip even though the GFM#1 secondary control set-point goes to $P_{\text{set}} = 1pu$. However, after the attack duration, the secondary controls operate normally to increase the GFM#2 and GFM#3 inverter outputs to bring the system frequency back to 60 Hz. It is important to observe that in the absence of DAC, during the attack duration, the system was operating beyond the safe region.

2.9.2 Results with DAC

In the case where the DAC is active along with the GFM droop during the cyber-attack, the DAC senses that the frequency goes beyond the safe limits during both events due to the set-point attack. The DAC then appropriately modifies the set-points to maintain the system frequency within the safe limits. In the case with DAC, Fig. 18(d) shows that the DAC acts even during the cyber-attack on the secondary control set-points that are compromised. In this case, the DAC adjusts the set-points ensuring that the frequency excursion is not beyond the safe limits. The purpose of the DAC is to ensure that the system operates within the safe operating region and therefore adjusts the set-points of the GFM inverters to just bring the system frequency inside the safe region, thereby demonstrating local resilience.

During normal operations, it is not obvious to include the DAC as there are no indications of unsafe operations; however, during an abnormal condition like a cyber-attack as described, the DAC's capability shines to provide attack resilience with the decentralized and autonomous nature of the DAC.

The different models used in the validation study and the observations made are included in Table 3.

2.10 Discussion and Conclusions

Over the recent decades, there has been a rapid evolution of technologies and increased deployment of power electronics-based inverters, especially GFM inverters. While many system-level controls aim at enhancing performance under normal operating conditions, this work presents safety-based DACs to enhance the system performance under normal and stressed conditions. The DAC operates when the system frequency goes beyond the safe limits. The DACs reside at the device level (at the GFM inverters) and come in between the secondary and primary controls in the hierarchy of controls. They only act by modifying the secondary control set points

Table 3: Description of the different use cases utilized in the validation study.

Case	# INVs, # DGs	Disturbance	Observation
Subsection 2.7 Control performance during transients	2 DGs, 3 GFMs and 2 GFLs	The system is islanded at t = 1s and the region 4 is disconnected. The microgrid 2 and 3 form a networked microgrid. Again, at t = 12s, region 4 is energized by the networked microgrid.	Frequency limits were maintained using DACs whereas it violates without DAC
Subsection 2.8 IEEE 1547 Compliance at GFL Inverters	3 DGs, 1 GFM and 3 GFLs	The system is islanded at t = 2s and the region 4 is disconnected. The Microgrid 2 and 3 form a networked microgrid. At 8s, the DGs are re-dispatched to bring the frequency of microgrids 2 and 3 to the nominal 60Hz. At t = 12s, region 4 is energized by the networked microgrid.	The DACs maintain the UF2 threshold **avoiding GFL tripping** whereas without DAC, all 3 GFLs trip.
Subsection 2.9 Cyber Attack on set-points dispatched by centralized control	2 DGs, 3 GFMs and 2 GFLs	Besides the disturbance created in Subsection IV-B, between t = 2s and t = 16s, there is an attack on the secondary control inverter set-points.	The DACs modify the attacked set-points to **achieve resiliency** whereas without DAC the attack results in larger frequency deviations and unintended control effort

to maintain the local frequency constraints, and otherwise just pass the secondary control set points to the inverters. The DACs work with the droop controls in a complementary manner to enhance the droop controller functionality during emergencies. The DAC is demonstrated as a safety-promoting resilience control and the safe limits can be adjusted along with the control parameters to enhance the effective utilization of the GFM resources.

The DAC is an effective way to maximize resource utilization that ensures the system does not go out of the safe region and in limiting cases can prevent a collapse of the system due to cascaded contingencies. In this work, a scenario is presented where DACs prevent IEEE 1547 compliant GFL inverters tripping during a large disturbance [2]. The key impact of the DAC is demonstrated with the maintenance of the system frequency within the safe limits when resources exist and help drive the system toward the safe limits with the needed urgency when there are large disturbances. The DAC relies on the resource nameplate details and local measurements to steer the GFM resources to enhance the full utilization of system resources. This enables the DAC to have a check in place that can override the secondary control if the system steers away from the safe region. Overall, the DAC enhances the GFM inverter capabilities and improves its

droop functionality. The proposed controls are applicable universally and the team will implement these controls by including other resources like GFL inverters. This work will also be explored for applications beyond microgrids in future studies.

References

[1] W. Du, F. K. Tuffner, K. P. Schneider, R. H. Lasseter, J. Xie, Z. Chen, B. Bhattarai, Modeling of grid-forming and grid-following inverters for dynamic simulation of large-scale distribution systems, IEEE Transactions on Power Delivery 36 (4) (2020) 2035–2045.

[2] IEEE Standard for Interconnection and Interoperability of Distributed Energy Resources with Associated Electric Power Systems Interfaces, IEEE Std 1547-2018 (Revision of IEEE Std 1547-2003) (2018) 1–138doi:10.1109/IEEESTD.2018.8332112.

[3] J. W. Busby, K. Baker, M. D. Bazilian, A. Q. Gilbert, E. Grubert, V. Rai, J. D. Rhodes, S. Shidore, C. A. Smith, M. E. Webber, Cascading risks: Understanding the 2021 winter blackout in Texas, Energy Research & Social Science 77 (2021) 1 – 10.

[4] M. Farrokhabadi, C. A. Cañizares, J. W. Simpson-Porco, E. Nasr, L. Fan, P. A. Mendoza-Araya, R. Tonkoski, U. Tamrakar, N. Hatziargyriou, D. Lagos, et al., Microgrid stability definitions, analysis, and examples, IEEE Transactions on Power Systems 35 (1) (2019) 13–29.

[5] Y. Xu, C.-C. Liu, K. P. Schneider, F. K. Tuffner, D. T. Ton, Microgrids for service restoration to critical load in a resilient distribution system, IEEE Transactions on Smart Grid 9 (1) (2016) 426 – 437.

[6] J. A. Taylor, S. V. Dhople, D. S. Callaway, Power systems without fuel, Renewable and Sustainable Energy Reviews 57 (2016) 1322–1336.

[7] A. Maulik, D. Das, Stability constrained economic operation of islanded droop-controlled DC microgrids, IEEE Transactions on Sustainable Energy 10 (2) (2018) 569 – 578.

[8] J. Schiffer, R. Ortega, A. Astolfi, J. Raisch, T. Sezi, Conditions for stability of droop-controlled inverter-based microgrids, Automatica 50 (10) (2014) 2457 – 2469.

[9] E. Barklund, N. Pogaku, M. Prodanovic, C. Hernandez-Aramburo, T. C. Green, Energy management in autonomous microgrid using stability-constrained droop control of inverters, IEEE Transactions on Power Electronics 23 (5) (2008) 2346 – 2352.

[10] S. Kundu, W. Du, S. P. Nandanoori, F. Tuffner, K. Schneider, Identifying parameter space for robust stability in nonlinear networks: A microgrid application, in: 2019 American Control Conference (ACC), IEEE, 2019, pp. 3111–3116.

[11] S. P. Nandanoori, S. Kundu, W. Du, F. K. Tuffner, K. P. Schneider, Distributed small-signal stability conditions for inverter-based unbalanced microgrids, IEEE Transactions on Power Systems 35 (5) (2020) 3981 – 3990.

[12] J. M. Guerrero, J. C. Vasquez, J. Matas, L. G. De Vicuña, M. Castilla, Hierarchical control of droop-controlled ac and dc microgrids—a general approach toward standardization, IEEE Transactions on industrial electronics 58 (1) (2010) 158–172.

[13] S. Kundu, S. Geng, S. P. Nandanoori, I. A. Hiskens, K. Kalsi, Distributed barrier certificates for safe operation of inverter-based microgrids, in: 2019 American Control Conference (ACC), IEEE, 2019, pp. 1042–1047.

[14] Y. Chen, J. Anderson, K. Kalsi, S. H. Low, A. D. Ames, Compositional set invariance in network systems with assume-guarantee contracts, in: 2019 American Control Conference (ACC), IEEE, 2019, pp. 1027–1034.

[15] Y. Zhang, J. Cortés, Distributed bilayered control for transient frequency safety and system stability in power grids, IEEE Transactions on Control of Network Systems 7 (3) (2020) 1476–1488.

[16] S. Kundu, K. Kalsi, Transient safety filter design for grid-forming inverters, in: 2020 American Control Conference (ACC), IEEE, 2020, pp. 1299 – 1304.

[17] D. Q. Mayne, J. B. Rawlings, C. V. Rao, P. O. Scokaert, Constrained model predictive control: Stability and optimality, Automatica 36 (6) (2000) 789–814.

[18] M. Almassalkhi, S. Brahma, N. Nazir, H. Ossareh, P. Racherla, S. Kundu, S. P. Nandanoori, T. Ramachandran, A. Singhal, D. Gayme, et al., Hierarchical, grid-aware, and economically optimal coordination of distributed energy resources in realistic distribution systems, Energies 13 (23) (2020) 6399.

[19] M. Nagumo, Über die lage der integralkurven gewöhnlicher differentialgleichungen, Proceedings of the Physico-Mathematical Society of Japan. 3rd Series 24 (1942) 551 – 559.

[20] F. Blanchini, Set invariance in control, Automatica 35 (11) (1999) 1747 – 1767.

[21] M. M. Nicotra, E. Garone, The explicit reference governor: A general framework for the closed-form control of constrained nonlinear systems, IEEE Control Systems Magazine 38 (4) (2018) 89–107.

[22] H. Brezis, On a characterization of flow-invariant sets, Communications on Pure and Applied Mathematics 23 (2) (1970) 261 – 263.

[23] K. P. Schneider, N. Radhakrishnan, Y. Tang, F. K. Tuffner, C.-C. Liu, J. Xie, D. Ton, Improving primary frequency response to support networked microgrid operations, IEEE Transactions on Power Systems 34 (1) (2018) 659 – 667.

[24] J. Elizondo, R. Y. Zhang, P.-H. Huang, J. K. White, J. L. Kirtley, Inertial and frequency response of microgrids with induction motors, in: 17th Workshop on Control and Modeling for Power Electronics (COMPEL), IEEE, 2016, pp. 1 – 6.

[25] W. H. Kersting, Radial distribution test feeders, IEEE Transactions on Power Systems 6 (3) (1991) 975–985.

[26] T. Ersal, C. Ahn, I. A. Hiskens, H. Peng, J. L. Stein, Impact of controlled plug-in evs on microgrids: A military microgrid example, in: 2011 IEEE power and energy society general meeting, IEEE, 2011, pp. 1–7.

[27] A. Papachristodoulou, J. Anderson, G. Valmorbida, S. Prajna, P. Seiler, P. A. Parrilo, SOSTOOLS: Sum of squares optimization toolbox for MATLAB, available from http://www.cds.caltech.edu/sostools (2013).

[28] J. F. Sturm, Using SeDuMi 1.02, a MATLAB toolbox for optimization over symmetric cones, Optimization methods and software 11 (1999) 625 – 653, software available at http://fewcal.kub.nl/sturm/software/sedumi.html.

[29] J. Bezanson, S. Karpinski, V. B. Shah, A. Edelman, Julia: A fast dynamic language for technical computing, arXiv preprint arXiv:1209.5145 (2012).

[30] B. Legat, C. Coey, R. Deits, J. Huchette, A. Perry, Sum-of-squares optimization in Julia, in: First Annual JuMP-dev Workshop, 2017.

[31] M. Yamashita, K. Fujisawa, M. Fukuda, K. Kobayashi, K. Nakata, M. Nakata, Latest developments in the SDPA family for solving large-scale SDPs, in: Handbook on semidefinite, conic and polynomial optimization, Springer, 2012, pp. 687 – 713.

[32] J. Dahl, Semidefinite optimization using MOSEK, in: International Symposium on Mathematical Programming, 2012.

[33] K. P. Schneider, C. Miller, S. Laval, W. Du, D. Ton, Networked microgrid operations: Supporting a resilient electric power infrastructure, IEEE Electrification Magazine 8 (4) (2020) 70–79.

[34] F. Norouzi, T. Hoppe, L. R. Elizondo, P. Bauer, A review of socio-technical barriers to smart microgrid development, Renewable and Sustainable Energy Reviews 167 (2022) 112674.

[35] R. H. Lasseter, Z. Chen, D. Pattabiraman, Grid-forming inverters: A critical asset for the power grid, IEEE Journal of Emerging and Selected Topics in Power Electronics 8 (2) (2019) 925–935.

[36] O. Palizban, K. Kauhaniemi, Hierarchical control structure in microgrids with distributed generation: Island and grid-connected mode, Renewable and Sustainable Energy Reviews 44 (2015) 797–813.

[37] Y. Gu, T. C. Green, Power system stability with a high penetration of inverter-based resources, Proceedings of the IEEE (2022).

[38] U. Muenz, S. Bhela, N. Xue, A. Banerjee, M. J. Reno, D. Kelly, E. Farantatos, A. Haddadi, D. Ramasubramanian, A. Banaie, Protection of 100% inverter-dominated power systems with grid-forming inverters and protection relays–gap analysis and expert interviews, Tech. rep., Sandia National Laboratory (2024).

[39] Y. Jiang, R. Pates, E. Mallada, Dynamic droop control in low-inertia power systems, IEEE Transactions on Automatic Control 66 (8) (2020) 3518–3533.

[40] S. Geng, I. A. Hiskens, Unified grid-forming/following inverter control, IEEE Open Access Journal of Power and Energy 9 (2022) 489–500.

[41] J. M. Guerrero, M. Chandorkar, T.-L. Lee, P. C. Loh, Advanced control architectures for intelligent microgrids—part i: Decentralized and hierarchical control, IEEE Transactions on Industrial Electronics 60 (4) (2012) 1254–1262.

[42] D. B. Rathnayake, M. Akrami, C. Phurailatpam, S. P. Me, S. Hadavi, G. Jayasinghe, S. Zabihi, B. Bahrani, Grid forming inverter modeling, control, and applications, IEEE Access 9 (2021) 114781–114807.

[43] Y. Khayat, M. Naderi, Q. Shafiee, Y. Batmani, M. Fathi, J. M. Guerrero, H. Bevrani, Decentralized optimal frequency control in autonomous microgrids, IEEE Transactions on Power Systems 34 (3) (2018) 2345–2353.

[44] Z. Lian, C. Wen, F. Guo, P. Lin, Q. Wu, Decentralized secondary control for frequency restoration and power allocation in islanded ac microgrids, International Journal of Electrical Power & Energy Systems 148 (2023) 108927.

[45] A. Singhal, T. L. Vu, W. Du, Consensus control for coordinating grid-forming and grid-following inverters in microgrids, IEEE Transactions on Smart Grid 13 (5) (2022) 4123–4133.

[46] J. Liu, H. Song, C. Chen, J. M. Guerrero, M. Liu, Y. Qu, Decentralized secondary frequency control of autonomous microgrids via adaptive robust l2-gain performance, IEEE Transactions on Smart Grid (2023).

[47] V. Veerasamy, L. P. M. I. Sampath, S. Singh, H. D. Nguyen, H. B. Gooi, Blockchain-based decentralized frequency control of microgrids using federated learning fractional-order recurrent neural network, IEEE Transactions on Smart Grid 15 (1) (2023) 1089–1102.

[48] M. Starke, B. Ollis, J. Hambrick, M. Chinthavali, Microgrids and power quality, https://www.energy.gov/sites/default/files/2019/11/f68/22-fupwg-fall-2019-starke.pdf, accessed: 04-01-2024.

[49] E. Weitenberg, Y. Jiang, C. Zhao, E. Mallada, C. De Persis, F. Dörfler, Robust decentralized secondary frequency control in power systems: Merits and tradeoffs, IEEE Transactions on Automatic Control 64 (10) (2018) 3967–3982.

[50] R. H. Lasseter, J. H. Eto, B. Schenkman, J. Stevens, H. Vollkommer, D. Klapp, E. Linton, H. Hurtado, J. Roy, Certs microgrid laboratory test bed, IEEE Transactions on Power Delivery 26 (1) (2010) 325–332.

[51] A. K. Bharati, V. Ajjarapu, A scalable multi-timescale t&d co-simulation framework using helics, in: 2021 IEEE Texas Power and Energy Conference (TPEC), IEEE, 2021, pp. 1–6.

[52] A. K. Bharati, V. Ajjarapu, Smtd co-simulation framework with helics for future-grid analysis and synthetic measurement-data generation, IEEE Transactions on Industry Applications 58 (1) (2021) 131–141.

[53] K. P. Schneider, X. Sun, F. Tuffner, Adaptive load shedding as part of primary frequency response to support networked microgrid operations, IEEE Transactions on Power Systems 39 (1) (2023) 287–298.

Pacific Northwest National Laboratory

902 Battelle Boulevard
P.O. Box 999
Richland, WA 99352
1-888-375-PNNL (7675)

www.pnnl.gov